



# Recent advances in imaging devices: image sensors and neuromorphic vision sensors

Wen-Qiang Wu, Chun-Feng Wang\*, Su-Ting Han, Cao-Feng Pan\* 

Received: 5 January 2024 / Revised: 15 February 2024 / Accepted: 16 February 2024 / Published online: 2 July 2024  
© Youke Publishing Co., Ltd. 2024

**Abstract** Remarkable developments in image recognition technology trigger demands for more advanced imaging devices. In recent years, traditional image sensors, as the go-to imaging devices, have made substantial progress in their optoelectronic characteristics and functionality. Moreover, a new breed of imaging device with information processing capability, known as neuromorphic vision sensors, is developed by mimicking biological vision. In this review, we delve into the recent progress of imaging devices, specifically image sensors and neuromorphic vision sensors. This review starts by introducing their core components, namely photodetectors and photonic synapses, while placing a strong emphasis on device structures, working mechanisms and key performance parameters. Then it proceeds to summarize the noteworthy achievements in both image sensors and neuromorphic vision sensors, including advancements in large-scale and high-resolution imaging, filter-free multispectral recognition, polarization sensitivity, flexibility, hemispherical designs,

and self-power supply of image sensors, as well as in neuromorphic imaging and data processing, environmental adaptation, and ultra-low power consumption of neuromorphic vision sensors. Finally, the challenges and prospects that lie ahead in the ongoing development of imaging devices are addressed.

**Keywords** Imaging devices; Photodetectors; Photonic synapses; Image sensors; Neuromorphic vision sensors

## 1 Introduction

Imaging technology plays an important role in our daily lives, industrial processes and military defense strategies, such as facial recognition, instrument monitoring, and stealth detection [1–4]. The evolution of smart cameras and machine vision in recent times has led to fresh requirements for imaging devices [5, 6]. Currently, there are two categories of imaging devices, one is conventional image sensors, and the other is innovative neuromorphic vision sensors inspired by the principles of biological vision. Based on these two types of imaging devices, distinct image recognition systems have emerged (Fig. 1) [7–11].

In conventional image recognition systems, image sensors serve as indispensable imaging components [12, 13]. In recent years, significant improvements have been made in image sensors to amend the limitations encountered in practical applications [14–17]. For example, conventional flat image sensor arrays necessitate complex multi-lens optical systems for imaging, resulting in increased system-level complexity and larger device dimensions, as shown in Fig. 1a(i). To overcome this challenge, curved image sensors have been developed, offering the ability to capture

W.-Q. Wu, C.-F. Wang\*

Institute of Microscale Optoelectronics, College of Materials Science and Engineering, Shenzhen University, Shenzhen 518060, China  
e-mail: cfwang@szu.edu.cn

S.-T. Han

College of Electronics and Information Engineering, Shenzhen University, Shenzhen 518060, China

C.-F. Pan\*

Institute of Atomic Manufacturing, Beihang University, Beijing 100191, China  
e-mail: pancaofeng@buaa.edu.cn

C.-F. Pan

Beijing Institute of Nanoenergy and Nanosystems, Chinese Academy of Sciences, Beijing 100083, China



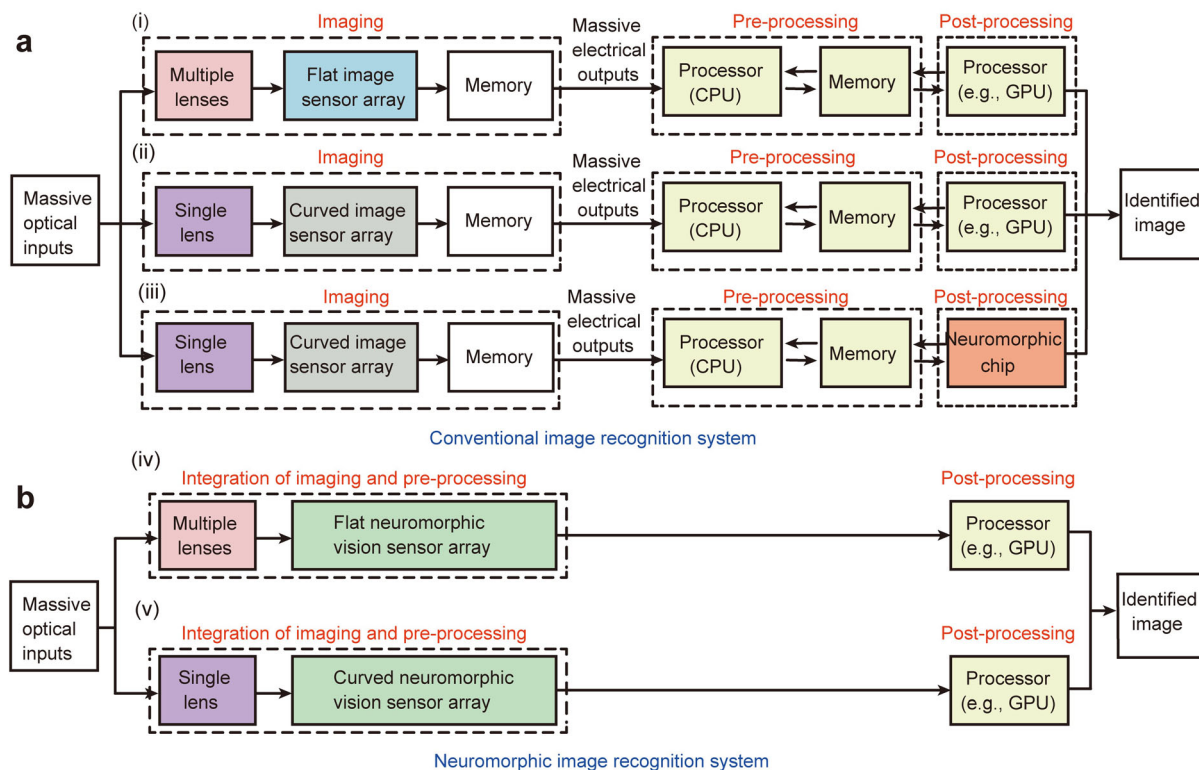


**Fig. 1** Image recognition systems: **a** conventional image recognition system based on image sensors. **b** Neuromorphic image recognition system based on neuromorphic vision sensors. Adapted with permission from Ref. [11]. Copyright 2022, Springer Nature

a wide field of view (Fig. 1a(ii)) [18, 19]. In addition, conventional image sensors often rely on intricate optical components, such as prisms or Bayer filters, to achieve wavelength discrimination [20]. Consequently, innovative filter-free narrowband image sensors have been devised through novel mechanisms, such as the charge collection narrowing (CCN) mechanism [21, 22]. Currently, image sensors are evolving towards achieving high-resolutions, large-scale and exceptional flexibility, among others [23–26]. Nevertheless, the conventional image recognition systems using image sensors and von Neumann’s computing architecture are inherently imperfect. Image sensors produce massive raw data in the entire time domain for frame-based image acquisition, bringing challenges to von Neumann architecture processors and resulting in high-energy consumption [27, 28]. Although neuromorphic processors with high processing efficiency are being developed, data communication among different modules, such as image sensors, memory and the central processing unit (CPU), still causes time delays (Fig. 1a(iii)) [29, 30]. Consequently, there is a growing need for advanced imaging devices that can seamlessly integrate both image acquisition and data processing.

Conversely, biological vision systems exhibit clear advantages over conventional image recognition systems, particularly when it comes to unstructured image

classification and recognition [31]. Inspired by the human visual system, a novel class of imaging devices known as neuromorphic vision sensors has been developed, integrating image acquisition and data processing (Fig. 1b) [9, 32, 33]. These neuromorphic vision sensors incorporate multiple light-modulated synaptic behaviors, such as spike-timing-dependent plasticity [34, 35]. Moreover, they have successfully realized advanced visual capabilities akin to biological vision, such as mixed-color pattern recognition and environmental adaptability [36–38].

Herein, recent advancements in imaging devices, specifically image sensors and neuromorphic vision sensors, are reviewed. We begin by introducing the device structures, working mechanisms, and key performance parameters of photodetectors and photonic synapses, which constitute the core components of image sensors and neuromorphic vision sensors, respectively. Next, we spotlight the progress in image sensor development, emphasizing achievements in terms of large-scale and high-resolution imaging, filter-free multispectral recognition, polarization sensitivity, flexibility, hemispherical designs and self-power supply. Subsequently, we provide a comprehensive overview of the notable accomplishments of neuromorphic vision sensors, encompassing their contributions to neuromorphic imaging and data processing, environmental adaptation and ultra-low power consumption. Finally, we

offer a concise summary and delve into the challenges and prospects for imaging devices.

## 2 Core components of imaging devices

### 2.1 Photodetectors

Photodetectors serve as the fundamental building blocks of image sensors [39]. In this section, we provide a comprehensive overview of photodetectors, focusing on their device structures, working mechanisms and the key performance parameters defining the functionality of image sensors.

#### 2.1.1 Device structures and working mechanisms

The photodetectors can be assigned into photoconductors, photodiodes, and phototransistors, each distinguished by their unique device structures and working mechanisms [40, 41]. A schematic representation of the structures of these three types of photodetectors is shown in Fig. 2.

Among these, the photoconductors with a metal–semiconductor–metal (MSM) configuration are the simplest in terms of structure. Depending on the positioning of electrodes on the semiconductor materials, photoconductors can be categorized into lateral and vertical structures, as shown in Fig. 2a. The working mechanism of photoconductors is based on the photoconductive effect [42, 43]. When photosensitive materials absorb photons with energy greater than their band gap, the free electron–hole pairs will be generated. Driven by an external electric field, the electron–hole pairs separate and move in the opposite direction to form a photocurrent. The photocurrent generated under light illumination can be calculated by the following equation [44]:

$$I = \frac{qNV}{L^2} (\tau_n \mu_n + \tau_p \mu_p) \quad (1)$$

where  $L$  is the width of the channel,  $qN$  represents the internal current generated by photoelectrons,  $V$  is working voltage,  $\mu_n$  and  $\mu_p$  represent the mobility of electron and hole, respectively, and  $\tau_n$  and  $\tau_p$  represent the lifetime of electron and hole pairs produced per unit time under illumination, respectively. In recent years, a variety of photoconductors have been fabricated based on novel semiconductor materials, such as zero-dimensional quantum dots (QDs), one-dimensional (1D) micro/nanowires, two-dimensional (2D) micro/nanosheets and film materials [45–49]. Owing to its relatively straightforward device assembly, the photoconductor is the most utilized component for the integration of image sensor arrays.

The photodiodes with a two-terminal structure are typically constructed using P–N junction or P–I–N junction materials, accompanying a built-in electric field, as shown in Fig. 2b [50, 51]. The photodiodes can operate in a self-powered mode based on the photovoltaic effect [52–54]. Under illumination, the electron–hole pairs can be generated within the semiconductor material when the absorbed energy surpasses the band gap threshold. The built-in electric field facilitates the movement of photogenerated electrons and holes in opposite directions, leading to the generation of a short-circuit current at zero bias. In addition, the photodiodes can also work in the presence of external voltage. In this case, it generally operates in the reverse bias state, in which the external electric field direction is consistent with the internal electric field, improving the efficiency of electron–hole pair separation. When an excessive reverse bias is applied, the avalanche multiplication of carriers may occur, which results in a large current gain or breakdown of the photodiodes. Si-based photodiodes are the most common P–N junction photodiodes in commercial complementary metal oxide

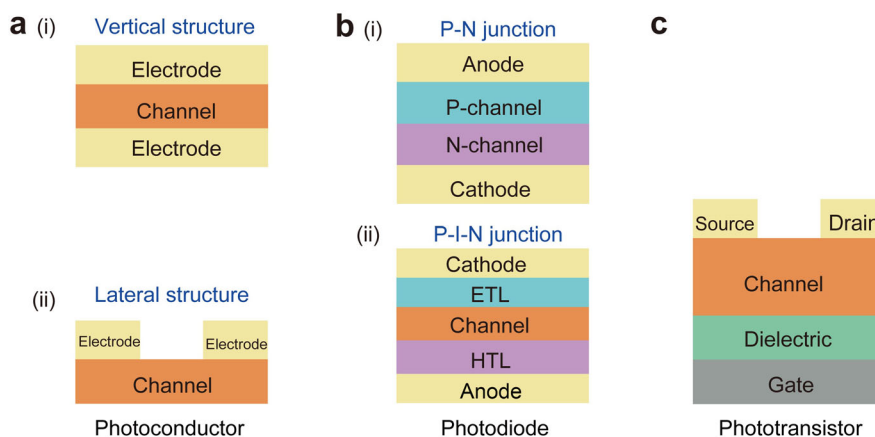


**Fig. 2** Schematic diagram of the structure of the photodetectors: **a** structural diagram of the photoconductor. **b** Structural diagram of the photodiode. **c** Structural diagram of the phototransistor

semiconductor (CMOS) image sensors [55, 56]. For the last few years, perovskite-based P–I–N junction photodiodes have been assembled and integrated as image sensors due to their excellent photoelectric properties [57, 58].

The phototransistors with a three-terminal structure combine the characteristics of transistors and photodiodes, as shown in Fig. 2c. Besides the source and drain electrodes, the phototransistor has an additional gate electrode, which can regulate the carrier density in the semiconductor channel [59]. Similar to photoconductors and photodiodes, phototransistors generate photocurrent when they absorb photons with energy exceeding the semiconductor's bandgap. By adjusting the gate voltage, the channel current can be modulated, allowing for the amplification of photocurrent or reduction of dark current. The structure of phototransistors determines the complexity of their array integration as image sensors. Traditional oxide film materials with high mobility, such as indium oxide ( $\text{In}_2\text{O}_3$ ) and indium gallium zinc oxide (IGZO), are frequently used to assemble phototransistors [60]. In addition, novel 2D materials are regarded as ideal candidates for fabricating phototransistors because of their excellent optoelectronic properties and easily modulated electrical properties by gate voltage. For example, wafer-scale 2D materials, such as molybdenum disulfide ( $\text{MoS}_2$ ), have been successfully synthesized and employed in the construction of image sensors [61].

### 2.1.2 Key performance parameters

**Responsivity ( $R$ )**  $R$  is defined as the ratio of photogenerated current to incident light power, which illustrates the photoelectric conversion capability of the photodetector. It can be shown as Eq. (2) [62]:

$$R = \frac{\Delta I}{P_{\text{in}}A} = \frac{I_{\text{light}} - I_{\text{dark}}}{P_{\text{in}}A} \quad (2)$$

where  $\Delta I$  is photogenerated current,  $P_{\text{in}}$  is incident light power density,  $A$  is the effective area of the photodetector,  $I_{\text{light}}$  and  $I_{\text{dark}}$  represent the current of the photodetector under illumination and at dark, respectively.

**External quantum efficiency (EQE)** EQE represents the proportion of collected charge carriers ( $N_c$ ) to the incident photons ( $N_i$ ) at a specific wavelength illumination. It is shown as Eq. (3) [63]:

$$\text{EQE} = \frac{N_c}{N_i} = \frac{hc}{e\lambda} \quad (3)$$

where  $h$ ,  $c$ ,  $e$  and  $\lambda$  represent the Planck constant, light speed, elementary charge and the wavelength of incident light, respectively.

**Noise equivalent power (NEP)** the detection limit of a photodetector is determined by its noise. NEP represents

the incident light power that yields a signal-to-noise ratio (SNR) of 1. The smaller the NEP is, the more the photodetector can detect weak light. It can be shown as Eq. (4) [64]:

$$\text{NEP} = \frac{i_n}{R} \quad (4)$$

where  $i_n$  is the noise current.

**Specific detectivity ( $D^*$ )**  $D^*$  is employed to evaluate the ability of photodetectors to detect the weakest light signals. It is inversely proportional to NEP and can be shown by Eq. (5a) [65]:

$$D^* = \frac{\sqrt{A\Delta f}}{\text{NEP}} = \frac{R\sqrt{A\Delta f}}{i_n} \quad (5a)$$

where  $\Delta f$  represents the electrical bandwidth. The noise sources of the photodetector mainly include shot noise,  $1/f$  noise, and thermal noise. To simplify the calculation formula,  $1/f$  noise and thermal noise are usually ignored. At this time, the shot noise from the dark current is the main noise of the photodetector. It can be shown as Eq. (5b) [66]:

$$D^* = \frac{R}{\sqrt{2eI_{\text{dark}}/A}} \quad (5b)$$

**Response speed** it is represented by response time, which can be divided into rising time ( $\tau_{\text{rise}}$ ) and falling time ( $\tau_{\text{fall}}$ ).  $\tau_{\text{rise}}$  is defined as the time that it takes to rise from 10% to 90% of the maximum current value.  $\tau_{\text{fall}}$  is defined as the time that it takes to fall from 90% to 10% of the maximum current value. The response speed is closely related to the transport and collection of charges, so reducing the electrode spacing helps to improve the response speed.

**Linear dynamic range (LDR)** LDR is a figure of merit that describes the linear relationship range between the photodetector's photogenerated current and the light intensity. It can be given by Eq. (6) [67]:

$$\text{LDR} = 20\lg \frac{P_{\text{max}}}{P_{\text{min}}} \quad (6)$$

where  $P_{\text{min}}$  and  $P_{\text{max}}$  represent the minimum light intensity and the maximum light intensity, respectively, in which the photogenerated current of the photodetector increases linearly with the light intensity.

**Photoconductive gain ( $G$ )**  $G$  is defined as the number of charge carriers that pass through the external circuit under each photon excitation. It can be quantitatively calculated by the ratio of photogenerated carrier lifetime ( $\tau_{\text{life}}$ ) to drift transit time ( $\tau_{\text{transit}}$ ) between two electrodes, which is shown by Eq. (7) [68]:

$$G = \frac{\tau_{\text{life}}}{\tau_{\text{transit}}} = \frac{\tau_{\text{life}}}{L^2} \mu_m V \quad (7)$$

where  $\mu_m$  is the mobility of the majority carrier.

## 2.2 Photonic synapses

Photonic synapses serve as the fundamental components of neuromorphic vision sensors. Unlike electronic synapses that generate action potentials in response to external voltage stimuli, photonic synapses produce action potentials in response to light signals [69–71]. In recent years, a plethora of innovative photonic synapses have been created for the development of neuromorphic vision sensors. In this section, we present an overview of the structure, working mechanism, and key performance parameters of photonic synapses.

### 2.2.1 Device structures and working mechanisms

The structure of photonic synapses falls into two categories: two-terminal structures and three-terminal structures [72]. Two-terminal photonic synapses share device structures similar to those of photoconductors and photodiodes, whereas three-terminal photonic synapses adopt the same structure as phototransistors. Compared with two-terminal photonic synapses, three-terminal photonic synapses usually have additional electrical modulation capacity for signal storage or recovery. It is essential to note that the working mechanisms and capabilities of photonic synapses diverge from those of photodetectors. Photodetectors can swiftly convert optical signals into electrical signals with rapid response and recovery times, but they cannot retain optical information once the light stimulus is removed. In contrast, photonic synapses, equipped with sensing and processing functions, possess the capacity for light-dependent memorization. Modulating the carrier transport and recombination processes is necessary to endow photonic synapses with biological synaptic behaviors. The working mechanisms of photonic synapses mainly include the introduction of trapping states, band arrangement engineering, and some special strategies [73–75].

The trapping states inside or at the interface of channel materials play an important role in the transport and recombination of charge carriers. Trapping states are undesired in the preparation of photodetectors. Reducing the presence of trapping states is conducive to rapid carrier transport for enhancing the photodetector's performance. However, the development of photonic synapses necessitates the deliberate incorporation of trapping states to emulate synaptic plasticity. There are three scenarios of trapping states existing in photonic synapses: defect states within the bulk of channel materials, defect states at the interface between two channel materials, and deliberately designed trapping layer. Oxide semiconductor films are known to harbor numerous oxygen vacancy defects, making them a common choice in the construction of photonic synapses. For example, Cao et al. demonstrated photonic synapses using

InSnZnO oxide semiconductor films modified by InP QDs [76]. The photonic synapses exhibited nonconstant current phenomena, ascribing to the carrier trapping and de-trapping by oxygen vacancy (Fig. 3a, b). During the device assembly processes, the defect states are sometimes introduced at the interface between different materials. For example, Kim et al. constructed a MoS<sub>2</sub>-organic heterostructure photonic synapse based on an interfacial defect trapping mechanism [11]. Time-dependent synaptic plasticity was proved relative to interfacial charge trapping between MoS<sub>2</sub> and dielectrics (poly(1,3,5-trimethyl-1,3,5-trivinyl cyclotrisiloxane)) (Fig. 3c, d). In addition, the deliberate introduction of a trapping layer is also an effective strategy for the preparation of photonic synapses. For example, Huang et al. demonstrated a photonic synapse by designing a polymethyl methacrylate (PMMA) film as a trapping layer between PbS QDs and pentacene [73]. Comparative experiments confirmed that the plasticity of synapses was contributed by the PMMA trapping layer (Fig. 3e, f).

Engineering the band alignment of two semiconductor materials is another way to regulate the carrier transport and recombination processes. In photonic synaptic devices, the principle of band alignment design should follow that electron–hole pairs can be separated quickly, in which one type of carrier is trapped in a selective channel material. The rapid separation of electron–hole pairs gives the photonic synapse rapid computing ability, while the trap of one type of carrier inhibits the recombination process to obtain memory function. Both type-I and type-II heterojunctions have been adopted in photonic synapses. Such a device generally requires the modulation of gate voltage, so it is usually a three-terminal device. Park et al. fabricated a photonic synapse based on the QDs/IGZO type-II heterojunction [74]. Under light stimulation, the photogenerated electron–hole pairs were generated within the QDs, the electrons were transferred to the IGZO film, while the holes were trapped in the QDs due to the barrier of energy band potential (Fig. 3g). When the light source was removed, the recombination process proceeded slowly because the holes trapped in the QDs, creating the memory function (Fig. 3h). Based on the above mechanisms, this device enabled fundamental synaptic behaviors, such as synaptic plasticity and non-volatile memory. In addition, the type-I heterojunction of carbon nitride (C<sub>3</sub>N<sub>4</sub>)/pentacene was applied in photonic synapses by Lee et al. [37]. To regulate the carrier transfer, an ultra-thin PMMA film was introduced as a tunneling layer between C<sub>3</sub>N<sub>4</sub> and pentacene. Under ultraviolet (UV) light illumination, the electron–hole pairs were generated in both C<sub>3</sub>N<sub>4</sub> and pentacene, and the holes in C<sub>3</sub>N<sub>4</sub> tunneled through PMMA film to pentacene, but the electrons were confined in C<sub>3</sub>N<sub>4</sub> (Fig. 3i). After the UV light was removed, the electron–hole pairs in pentacene rapidly recombined, whereas the electrons trapped

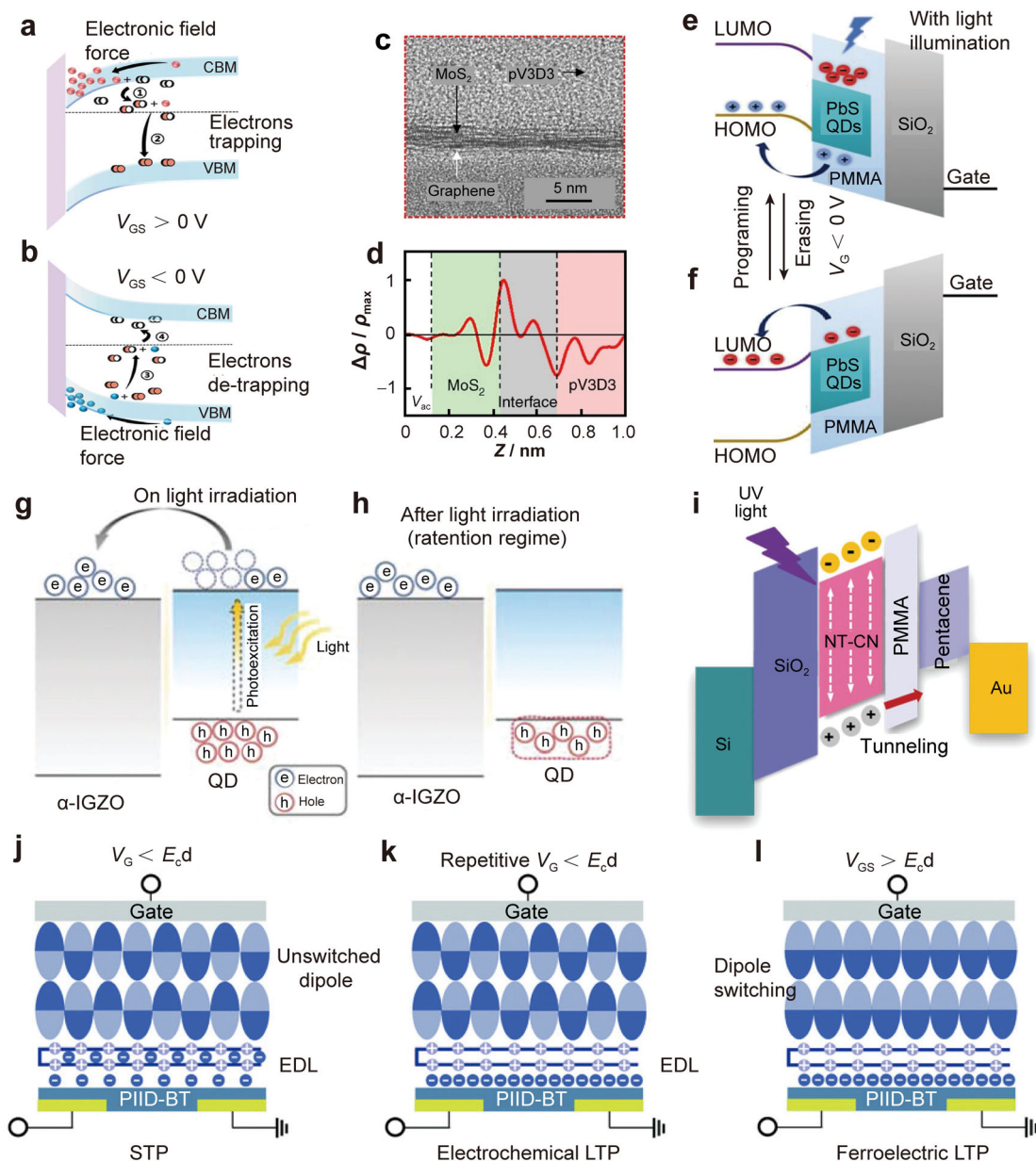


**Fig. 3** Schematic diagram of the working mechanism of photonic synapses: **a, b** oxygen vacancy defect states. Reproduced with permission from Ref. [76]. Copyright 2023, Wiley–VCH. **c, d** Interface defect states between two materials. Reproduced with permission from Ref. [11]. Copyright 2022, Springer Nature. **e, f** Deliberately designed trapping layer. Reproduced with permission from Ref. [73]. Copyright 2023, Wiley–VCH. **g, h** Type-II band arrangement. Reproduced with permission from Ref. [74]. Copyright 2022, Wiley–VCH. **i** Type-I band arrangement. Reproduced with permission from Ref. [37]. Copyright 2020, Wiley–VCH. **j–l** The ferroelectric/electrochemical modulated method. Reproduced with permission from Ref. [77]. Copyright 2018, Wiley–VCH

in  $C_3N_4$  slowly recombined with the holes. Based on the above type-I heterojunctions, the UV-response synaptic behaviors were successfully shown.

In addition, there are some special strategies to regulate carrier transport and recombination for photonic synapses. Chai et al. demonstrated a valence change switching mechanism in optoelectronic resistive random access memory (ORRAM) synaptic devices [75]. It involves the photogenerated electron–hole pairs and the protons ( $H^+$ )

produced by the reaction between the photogenerated holes and the absorbed water molecules in the  $MoO_x$  films. Under illumination, the photogenerated electrons and protons caused the valence state of Mo ions to change from  $6^+$  to  $5^+$ , which resulted in the resistance state of  $MoO_x$  films changing from a high resistance state (HRS) to a low resistance state (LRS). During the reset processes, the proton was extracted from  $MoO_x$  films driven by the electric field, and the valence state of Mo ion was restored

from  $5^+$  to  $6^+$ , causing the resistance state to return from LRS to HRS. The light dosage (light intensity and illumination time) influenced the reaction of protons and  $\text{Mo}^{5+}$ . The device exhibited light-dependent synaptic behaviors and nonvolatile memory characteristics. Liu et al. proposed a ferroelectric/electrochemical modulated approach for organic synapse [77]. The amplitude, frequency and duration time of gate voltage play a vital role in synaptic plasticity. When the gate voltage was lower than the coercive voltage ( $V_c$ ) of ferroelectric materials, mobile counter anions (ethyl sulfate in P(VP-EDMAEMAES)) were doped into PIID-BT driven by an electrostatic field. The electric double layer (EDL) and the hole channel were formed (Fig. 3j). Repetitive or long-term gate voltage stimulation produced changes from electrochemical short-term plasticity to long-term plasticity (Fig. 3k). Furthermore, when the gate voltage surpassed the  $E_c$ , the ferroelectric long-term plasticity was established, producing a nonvolatile current (Fig. 3l). As a proof-of-concept, a neuromorphic vision sensor was constructed and exhibited nonvolatile plasticity of 10,000 s persistent and unique threshold switching characteristics.

### 2.2.2 Key performance parameters

*Synaptic weight* in biological neural networks, the synapse is the connection between two neurons that can transmit information. The synaptic weight is expressed by the connection strength between preneurons and postneurons [78]. In photonic synapses, synaptic weight refers to the conductivity of the device channel [79].

*Synaptic plasticity* the change in synaptic weight refers to synaptic plasticity. In biology, synaptic plasticity underlies learning and memory in the human brain [80]. Synaptic plasticity can be divided into two categories: short-term synaptic plasticity and long-term synaptic plasticity. Short-term synaptic plasticity usually lasts for very short periods of milliseconds to seconds [81]. Long-term synaptic plasticity refers to changes in synaptic weights lasting a long time (a few minutes to weeks or even longer) [82, 83]. According to whether synapses are excitatory or inhibitory, synaptic plasticity can be divided into short-term potentiation (STP)/long-term potentiation (LTP) and short-term depression (STD)/long-term depression (LTD) [84]. Repetitive stimulation or prolonged stimulation can lead to a transition in synaptic behavior from STP/STD to LTP/LTD.

*Paired-pulse facilitation/paired-pulse depression (PPF/PPD)* PPF/PPD as a fundamental characteristic of short-term synaptic plasticity describes the facilitation/depression ability of a synapse when it receives two consecutive stimulus signals. The amplitude of the first current peak is

defined as  $A_1$ , while the second one is defined as  $A_2$ . PPF/PPD index can be calculated by the Eq. (8) [85]:

$$\text{PPF/PPD} = \frac{A_2}{A_1} \times 100\% \quad (8)$$

where the amplitude of the second current peak ( $A_2$ ) is larger than the first one ( $A_1$ ), and the PPF/PPD index will decrease as the time interval between the two successive synapses increases. The relationship between the PPF/PPD index and the time interval can be fitted with different functions, the most common of which is the double exponential decay function as Eq. (9) [86]:

$$\text{PPF/PPD decay} = c_1 \exp\left(-\frac{\Delta t}{\tau_1}\right) + c_2 \exp\left(-\frac{\Delta t}{\tau_2}\right) \quad (9)$$

where  $\Delta t$  represents the pulse time interval,  $\tau_1$  and  $\tau_2$  are the characteristic relaxation time of the fast phase and the slow phase,  $c_1$  and  $c_2$  are the initial facilitation/depression magnitudes of respective phases.

*Energy Consumption* Energy consumption of photonic synapses is a key concern for the development of neuromorphic vision sensors. Generally, the energy consumption of photonic synapses can be divided into electrical energy consumption ( $E_e$ ) and optical energy consumption ( $E_l$ ).  $E_e$  and  $E_l$  of a synaptic event can be calculated by Eq. (10) [87]:

$$E_e = \int_{t_0}^{t_0+\Delta t} V \times I(t) \times dt \approx V \times I_{t_0+\Delta t} \times \Delta t \quad (10)$$

where  $t_0$  is the time when the light pulse starts,  $\Delta t$  represents the duration time of a light pulse,  $V$  is the working voltage,  $I_{t_0+\Delta t}$  is the current at the end of the light pulse.

$$E_l = P \times S \times \Delta t \quad (11)$$

where  $P$  and  $S$  represent the optical power density and the effective illumination area of the device.

## 3 Development of high-performance imaging devices

### 3.1 Image sensors

The increasing requirement of image information acquisition is the primary impetus behind the development of novel image sensors. Considerable efforts have been devoted to improving the performance of image sensors through the synthesis of new materials and the innovation of device structures [8, 88–91]. This ongoing endeavor has yielded significant advancements in device structure, functionality, and power efficiency [17, 92, 93]. In this

**Table 1** Summary of characteristics and functions of recently reported advanced image sensors

Device	Fabrication strategy	Material	Pixel number	Function	Refs.
Large-scale and high-resolution image sensors	Crossbar structure	ITO/NiOx/MAPbI <sub>3</sub> /C60/BCP/Ag	48 × 48	Large-scale imaging	[94]
	Crossbar structure	ITO/ZnO/Ag	4 × 4	Ultrahigh-resolution imaging	[96]
	Using CMOS backplanes	PCDTBT/PCBM	640 × 480	Fingerprint scanning	[97]
	Using CMOS backplanes	MAPbI <sub>3</sub>	640 × 480	Ultrahigh-resolution X-ray imaging	[98]
Filter-free multispectral image sensors	Integrating different bandgap materials	PbS/CdSe QDs	10 × 10	Multispectral recognition	[99]
	Constructing narrowband devices	Perovskites	32 × 32	Panchromatic imaging	[102]
Polarization-sensitive image sensors	Designing a special geometry structure	Moiré-lattices MAPbI <sub>3</sub>	Single	Polarization imaging	[107]
	Using structural anisotropic materials	GeS <sub>2</sub>	Single	UV polarization-sensitive detection	[109]
	Using structural anisotropic materials	BP	Single	NIR polarization-sensitive detection	[110]
	Using structural anisotropic materials	(iso-BA) <sub>2</sub> PbI <sub>4</sub>	Single	Vis polarization-sensitive detection	[112]
High-flexible image sensors	Using ultrathin substrate and encapsulation layer	CsPbBr <sub>3</sub>	10 × 10	Bending and compression; Retina-like imaging	[121]
	Using flexible photosensitive material and substrate	SnS QDs/Zn <sub>2</sub> SnO <sub>4</sub> nanowires	10 × 10	Bending; broadband imaging	[122]
Hemispherical image sensors	Ultra-thin design	Organic material	12 × 12	Hemispherical focal plane imaging	[123]
	Island-bridge structure	MoS <sub>2</sub> -graphene	1500	Imaging in the soft retinal implant	[124]
	Origami structure	Silicon	676	Artificial compound eye	[125]
	Hemispherical template	FAPbI <sub>3</sub> nanowires	100	Wide-angle imaging	[126]
Self-powered image sensors	Type-II heterojunction	Si/Se	3 × 3	0 V, Vis light imaging	[131]
	P–N junction	GaSe <sub>2</sub> /GaN	4 × 4	0 V, UV light imaging	[132]
	P–I–N junction	TiO <sub>2</sub> /CsPbBr <sub>3</sub> /Spiro-OMeTAD	arrays	0 V, Vis light imaging	[57]
	Schottky junction	Pt/Ga <sub>2</sub> O <sub>3</sub> /ITO	5 × 5	0 V, deep-UV light imaging	[133]

section, we primarily delve into the advancements in image sensors, focusing on their evolution towards large-scale and high-resolution imaging, filter-free multispectral recognition, polarization sensitivity, high flexibility, hemispherical designs and self-power supply. A comparison of the characteristics and functions of the latest reported image sensors is shown in Table 1 [57, 94, 96–99, 102, 107, 109, 110, 112, 121–126, 131–133].

### 3.1.1 Large-scale and high-resolution imaging

Achieving both high-resolution and large-scale is fundamental for image sensors to capture precise image information. One strategy for constructing high-resolution and large-scale image sensors is to employ crossbar-structured arrays with the photodetector sandwiched between cross electrodes. Compared with the planar electrode structure, this strategy offers the advantage of reducing the number of

electrodes for an array device from  $m \times n + 1$  to  $m + n$  ( $m$  and  $n$  are the number of pixels in the row and column of an image sensor). To reduce crosstalk between pixels, single-pass photodiodes are generally employed in such crossbar-structured devices. Pan et al. reported a high-resolution perovskite-based image sensor with a vertical crossbar structure (Fig. 4a) [94]. Since, the perovskite material is not compatible with the photolithography process, the top electrodes of this kind of device are usually prepared by a shadow mask, which seriously limits the device's resolution. In this work, the top electrode arrays with a width of 50  $\mu\text{m}$  were prepared by introducing waterproof parylene-C films and subsequent etching enabled by inductively coupled plasma (ICP). This approach yielded a  $48 \times 48$  image sensor with a resolution of 317 pixels per inch (PPI). Each pixel possesses a photodiode-type configuration of indium tin oxide (ITO)/nickel oxide ( $\text{NiO}_x$ )/ $\text{MAPbI}_3$  ( $\text{MA} = \text{CH}_3\text{NH}_3$ )/fullerenes (C60)/bathocuproine (BCP)/Ag (Fig. 4b)). Benefiting from the presence of the built-in electric field and the uniform photoelectric performances, the prepared device achieved high-resolution imaging at a voltage of 0 V (Fig. 4c, d). It's worth noting that existing silicon-based image sensors typically have a resolution of over 1  $\mu\text{m}$  [95]. Thus, there is a growing interest in achieving nanoscale resolution for advanced digital image sensors. Jiang and Song [96] prepared an ultrahigh-resolution image sensor with a pixel size of 50 nm. A crossbar structure was constructed by vertical ZnO nanorod arrays, ITO film and gold film serving as light-sensitive material, top and bottom electrodes, respectively (Fig. 4e, f). The device surpasses the resolution limit of existing commercial image sensors. Unfortunately, the extremely time-consuming technology of electron-beam lithography was required during the device processing, resulting in a device with only  $4 \times 4$  pixels, which is far from large-scale integration.

The combination of light-sensitive materials with CMOS backplanes is another effective strategy for preparing high-resolution and large-scale image sensors. Using such an approach, Gelinck et al. [97] fabricated an image sensor comprising  $640 \times 480$  pixels with a resolution of 508 PPI (Fig. 4g). The backplane is a dual-gate self-aligned oxide thin-film transistor (TFT) array. The organic materials of a p-type semiconductor, poly[N-9'-heptadecan-2,7-carbazolealt-5,5-(4',7'-di-2-thienyl-2',1',3'-benzothiadiazole)] (PCDTBT) and an n-type semiconductor, 6,6-phenyl-C61-butyric acid methyl ester (PCBM) were mixed into bulk heterojunction as photosensitive materials. Owing to ultra-high-resolution, this device can be used as an optical fingerprint scanner. Fingerprint scanning was performed in reflection mode by applying a beam of backlight irradiation. A clear fingerprint image was

obtained, and the contrast and sharpness of the image were further increased by correction (Fig. 4h, i). The obtained image enables to resolution of pores, fully illustrating the ultra-high-resolution of the prepared image sensor. Through the same strategy, Tedde et al. demonstrated a high-resolution X-ray image sensor with metal halide perovskites [98]. An IGZO TFT array comprising  $640 \times 480$  pixels with a resolution of 508 PPI was used as a backplane. This detector exhibited extremely high imaging spatial resolution of 6 line pairs per millimeter.

### 3.1.2 Filter-free multispectral recognition

Image sensors equipped with multispectral recognition functions can capture both the contour and color information of an object, rendering them more versatile and valuable compared to monochromatic image sensors. At present, multispectral imaging technology predominantly relies on broadband image sensors in conjunction with specialized color filters, which significantly constrain the feasibility of achieving large-area, high-resolution and flexible imaging. Therefore, there is an urgent need for the development of filter-free multispectral image sensors.

The monolithic integration of multiple semiconductor materials with different bandgaps is a method for preparing filter-free multispectral image sensors. Park et al. reported a filter-free multispectral image sensor by monolithically integrated QDs with IGZO phototransistors (Fig. 5a) [99]. The architecture of the device and interface properties between photosensitive materials was specially designed for high sensitivity. IGZO-based TFT was used to prepare the large-area and active-matrix devices due to their high carrier mobility, low off-state current and scalability. Four QD materials (10 nm PbS QDs, 7 nm CdSe QDs, 5 nm CdSe QDs and 3 nm CdS QDs) with bandwidth from visible (Vis) to near-infrared (NIR) were employed for spectral discrimination (Fig. 5b). The patterning of QDs layers used  $\text{Sn}_2\text{S}_6^{4-}$  ligands with high photochemical reactivity instead of conventional photoresists. The highly conductive chelating chalcometallate ligands promoted efficient transport of photogenerated carriers. The device exhibited extremely high photodetectivity over  $4.2 \times 10^{17}$  Jones at a white light intensity of  $1.36 \text{ mW}\cdot\text{cm}^{-2}$ , which is the highest value in solution-processed organic and QD image sensors so far. Under the illumination of five light sources with different wavelengths, 2D areal mapping of output currents was successfully obtained through the image sensor, revealing its full-color imaging capability (Fig. 5c–g). In this work, the device pixel arrays were integrated laterally, which constrained geometric fill factors and were not conducive to high-resolution imaging and compact sensing systems. Park's group further constructed

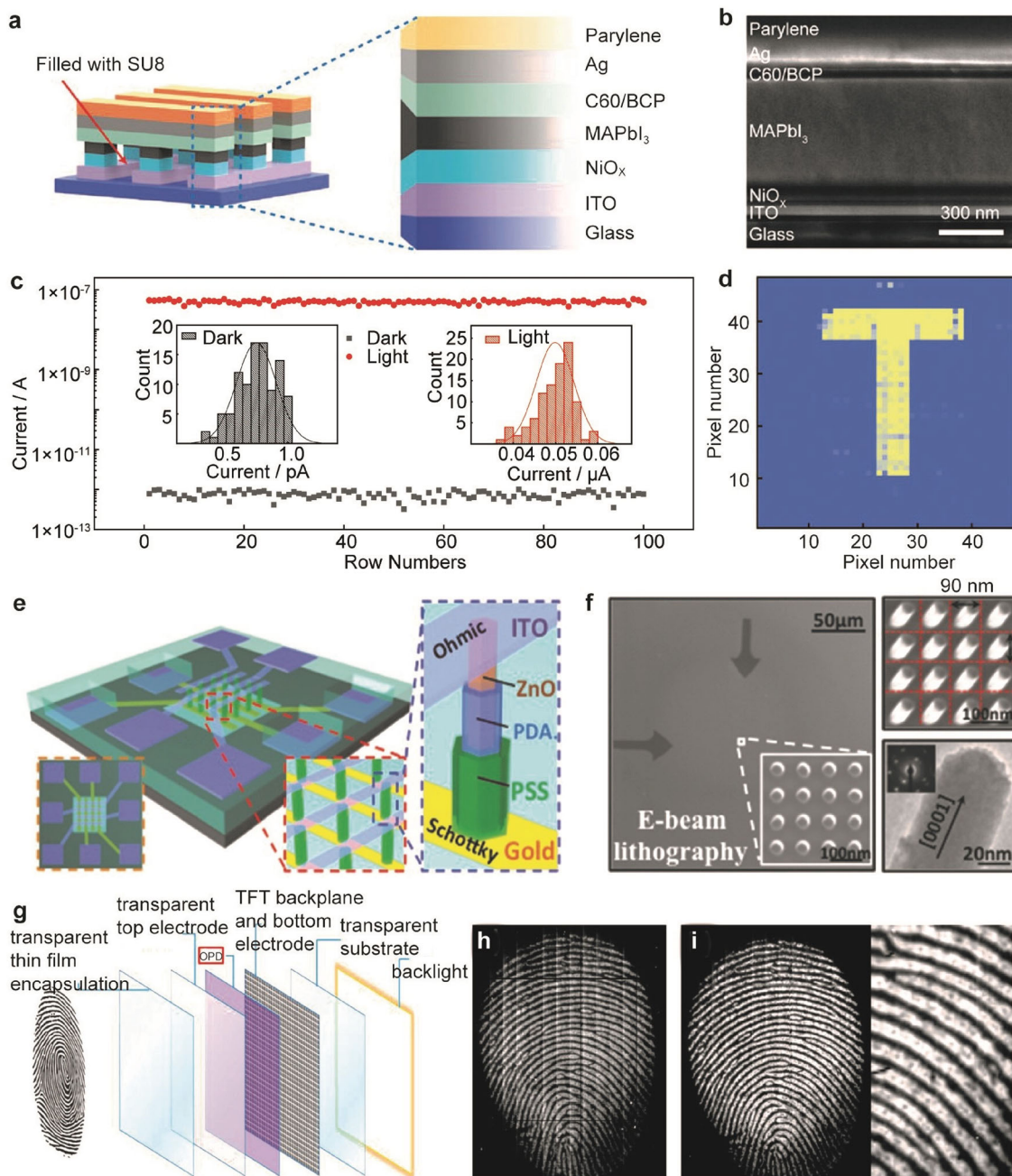


**Fig. 4** Large-scale and high-resolution image sensors: **a**, **b** structural diagrams of the large-scale and high-resolution perovskite image sensor and the cross-section SEM image of an individual pixel. **c** Statistical results of photocurrent and dark current of 100 pixels. **d** High-resolution imaging results of the device. Reproduced with permission from Ref. [94]. Copyright 2023, Wiley-VCH. **e**, **f** Structural diagram and corresponding SEM images of ultra-high-resolution image sensor. Reproduced with permission from Ref. [96]. Copyright 2015, Wiley-VCH. **g** Structural diagram of the large-scale and high-resolution X-ray image sensor. **h**, **i** Photograph of high-resolution fingerprint imaging. Reproduced with permission from Ref. [97]. Copyright 2019, Wiley-VCH

vertically stacked multispectral image sensors [100]. Three vertically stacked QDs materials were located on top of the IGZO film transistors to identify red (R), green (G) and blue (B) lights. Compared with the traditional laterally arranged structure, the vertically stacked structure improved the resolution of the image sensor.

In addition, filter-free narrowband photodetectors could be integrated as multispectral image sensors [101]. Mimicking human retinal photoreceptors, Wang et al. [102] constructed R/G/B narrowband image sensors based on perovskite films (Fig. 5h). The principle of narrowband detection is based on unbalanced electron-hole mobility

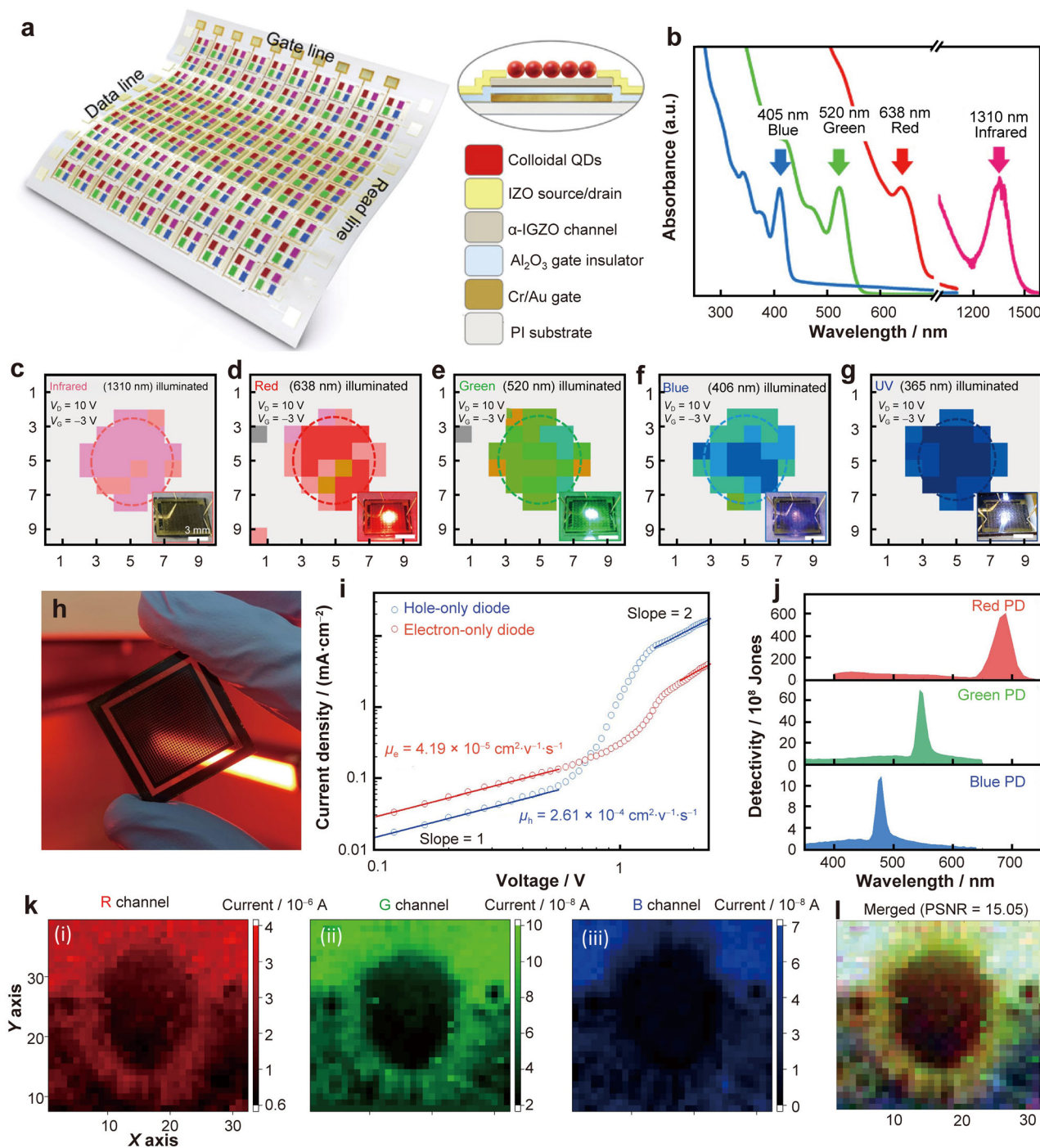


**Fig. 5** Filter-free multispectral image sensors: **a** schematic illustration of the full-color image sensor assembled by monolithically integrating different QDs with TFT transistors. **b** Absorption spectra of different QD materials. **c–g** The imaging results of the device under different color lights. Reproduced with permission from Ref. [99]. Copyright 2019, Amer Assoc Advancement Science. **h** Photograph of a perovskite narrowband image sensor. **i** Current density–voltage curves of the electron-only diode and hole-only diode measured in the dark. **j** Spectral photoresponse of R-, G-, B-narrowband image sensors. **k** The imaging results of R-, G-, and B-narrowband image sensors. **l** The image merged by R-, G-, and B-channel. Reproduced with permission from Ref. [102]. Copyright 2023, Amer Assoc Advancement Science

( $\mu_h > \mu_e$ ) of perovskite films in P–I–N configuration. Charge transport properties were investigated by monotype carrier-type diodes, indicating that the  $\mu_h$  of perovskites

synthesized with the volatile solvent method is much greater than  $\mu_e$  (Fig. 5i). By engineering the composition of perovskite materials, R/G/B narrowband image sensors

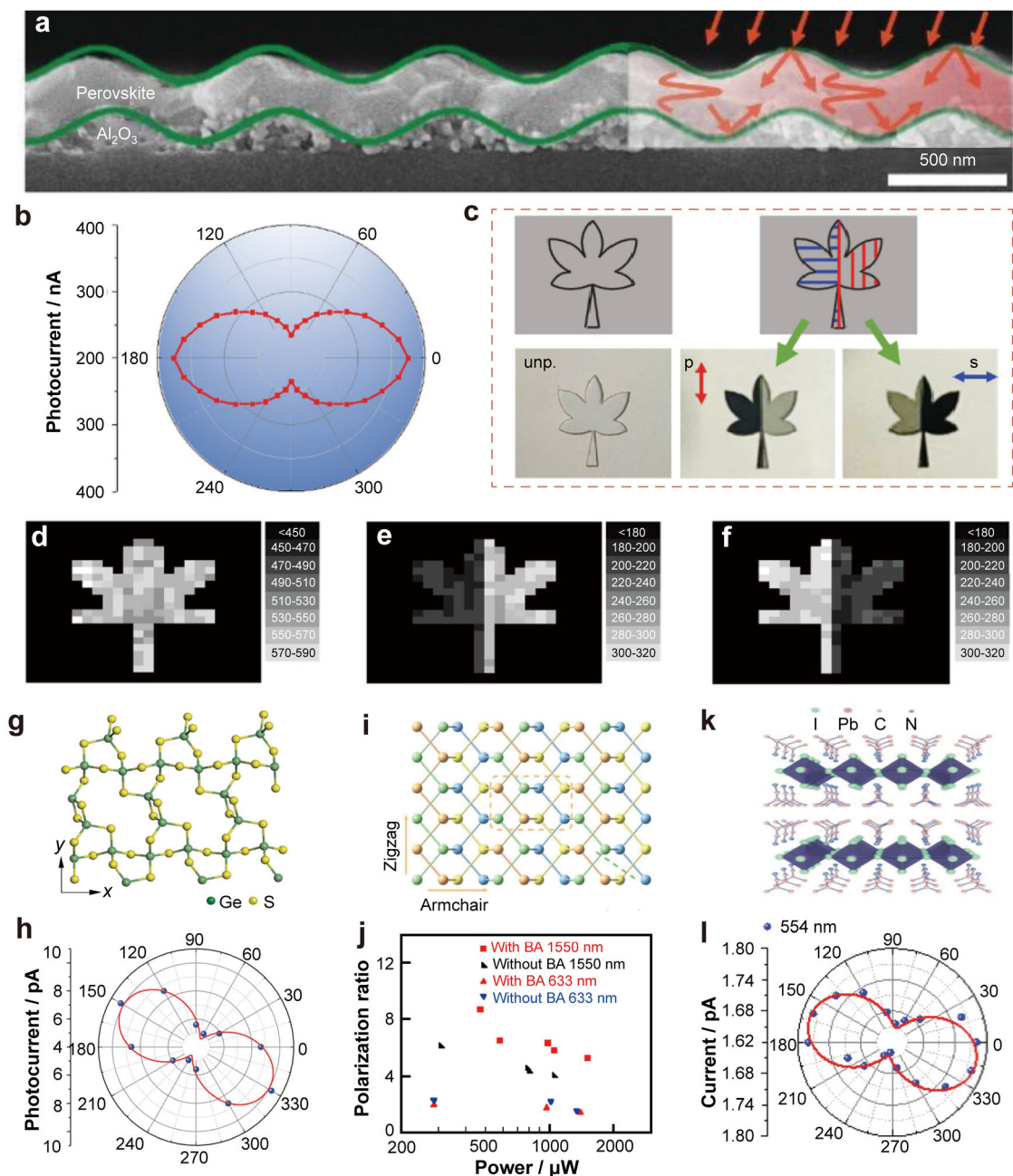


**Fig. 6** Polarization-sensitive image sensors: **a** SEM image of perovskite film with a stacked dual shallow grating structure. **b** Photocurrent of the device under different polarization angles. **c** Schematically illustration of the unpolarized light and different polarized light. Reproduced with permission from Ref. [107]. Copyright 2021, Wiley-VCH. **d–f** Imaging results of the image sensor under unpolarized light, p-polarized light, and s-polarized light. **g** Crystal structure diagram of GeS<sub>2</sub>. **h** Photocurrent of the image sensor under different polarization angles. Reproduced with permission from Ref. [109]. Copyright 2019, Wiley-VCH. **i** Crystal structure diagram of BP. Reproduced with permission from Ref. [111]. Copyright 2020, Wiley-VCH. **j** Comparing the polarization ratio of different devices with and without bowtie apertures. Reproduced with permission from Ref. [110]. Copyright 2018, American Chemical Society. **k** Crystal structure diagram of (iso-BA)<sub>2</sub>PbI<sub>4</sub>. **l** The photocurrent versus the polarization angle. Reproduced with permission from Ref. [112]. Copyright 2019, Wiley-VCH

achieved narrow photoresponse in the R, G and B regimes, respectively (Fig. 5j). In addition, the authors constructed R/G/B image sensor chips for panchromatic imaging, where each chip as an individual channel only detected the

corresponding color without any interference with others. The 2D photocurrent mapping of a yellow sunflower was obtained successfully from the corresponding chip (Fig. 5k). A panchromatic sunflower was reconstructed by

channel merging, illustrating the capability of the R/G/B narrowband image sensor for multispectral imaging (Fig. 5l).

### 3.1.3 Polarization sensitivity

Polarization light contains more optical information than natural light, such as polarization direction, polarization ellipticity and rotation direction [103]. These polarization properties could be characterized by polarization-sensitive image sensors. In recent years, polarization-sensitive image sensors have received wide attention due to their significance in geological remote sensing, optical radar, medical examination and other fields [104–106]. The assembly of polarization-sensitive image sensors can use semiconductor materials either with special geometry morphology or structural anisotropy.

The construction of special geometry morphology requires complex patterning techniques. Li et al. reported a polarization-sensitive image sensor based on moiré-lattices perovskite with a stacked dual shallow grating structure (Fig. 6a) [107]. Such structured perovskite film was fabricated by nanoimprint technology using a low-cost commercial digital versatile disc. This special structure endowed the device with unique light-harvesting capabilities, such as antireflection properties at the top grating, enhanced light reflection at the bottom grating, light capture from light diffraction and excitation of waveguide modes. As shown in Fig. 6b, this device exhibited the ability to detect polarized light. The photocurrent of the device changed with the polarization direction of the applied linearly polarized light. The maximum and minimum photocurrents appeared in the polarization directions at 0° and 90° with a peak-to-valley ratio of 1.58. Unpolarized light, p-polarized light and s-polarized light were employed for the demonstration of polarization imaging (Fig. 6c). The polarization-sensitive image sensor realized polarization imaging that accords with the polarization direction of the incident light (Fig. 6d–f).

Semiconductor materials with structural anisotropy, such as orthogonality, monoclinic, and triclinic, can be directly applied to polarization-sensitive image sensors. In recent years, large amounts of 2D materials with low symmetry lattice structures, such as black phosphorus (BP), germanium disulfide ( $\text{GeS}_2$ ), molybdenum telluride ( $\text{MoTe}_2$ ) and palladium diselenide ( $\text{PdSe}_2$ ), were investigated [108]. Hu et al. reported the polarization-sensitive UV photodetector based on  $\text{GeS}_2$  [109]. Theoretical band calculations were performed to research the structure of  $\text{GeS}_2$  along the  $x$  and  $y$  axes, revealing its in-plane anisotropic band structure (Fig. 6g). The photoresponse of the  $\text{GeS}_2$  photodetector presented angle-dependent characteristics, which can be plotted by a two-leaf graph and

conformed to the sinuous function (Fig. 6h). This result is consistent with the polarization-resolved absorption spectra of  $\text{GeS}_2$ , indicating that this is its intrinsic linear dichroic photoresponse. The dichroic ratio of the  $\text{GeS}_2$  photodetector is 2.1, which is the first reported polarization-sensitive UV photodetector based on anisotropic 2D materials. Xu et al. reported the NIR polarization-sensitive photodetector based on BP [110]. BP with a puckered layer structure has anisotropic in-plane properties along its two principal armchair and zigzag directions, where absorption in the armchair direction is stronger than that in the zigzag direction (Fig. 6i) [111]. In this work, the author employed plasmonic resonance to enhance polarization-sensitive photodetection. A high polarization degree (armchair to zigzag) of 8.7 was obtained at 1550 nm, which is of great value in infrared polarization detection (Fig. 6j). In addition, 2D layered metal halide perovskite materials are also a kind of promising semiconductor materials widely used in polarization detection. Li et al. demonstrated the 2D perovskite polarization-sensitive photodetector [112]. Figure 6k graphically shows the structure of  $(\text{iso-BA})_2\text{PbI}_4$  single crystals, in which each layer of inorganic  $[\text{PbI}_6]^{4-}$  octahedral is sandwiched by organic cations of iso-butylamine. The reflection spectra revealed the anisotropy of the  $(\text{iso-BA})_2\text{PbI}_4$  single crystals, and the linear dichroic ratio, defined as the ratio of the maximum reflection intensity to the minimum reflection intensity, was about 1.45. Owing to the anisotropy of the 2D perovskite lattice structure, the device realized the filter-less polarization detection with a linear dichroic ratio of 1.56 under the oblique incident angle of 45° (Fig. 6l). Although semiconductors with structural anisotropy are widely used in polarization detection, the array device of polarization-sensitive image sensors based on these materials are rarely reported because such materials are difficult to be controllably prepared in a large area.

### 3.1.4 High flexibility

As wearable technology continues to evolve, the demand for mechanically flexible image sensors is rapidly increasing, particularly in medical and security applications [14, 113, 114]. In contrast with conventional image sensors on rigid substrates, mechanical flexibility helps minimize performance attenuation under associated stress and deformation, which allows for new functions such as implantable applications [62, 115]. The key focus in developing flexible image sensors lies in the selection of photosensitive materials and substrates. Organic materials have attracted much attention due to their lightweight and high flexibility [116]. Some inorganic materials, such as 1D nanowires and thin films, are also used [117–120]. The flexible substrates commonly used are polyethylene

terephthalate (PET), poly(ethylene-2, 6-naphthalate (PEN), polyimide (PI) and parylene-C [8]. Pan's group fabricated an ultra-flexible image sensor with CsPbBr<sub>3</sub> perovskite materials on a parylene-C substrate (Fig. 7a–c) [121]. The device possessed the characteristics of ultralight weight and conformable contact (Fig. 7d). Owing to its excellent flexibility, the device still worked normally under bending deformation or being compressed by 50%. After 5000 bending cycles, the image sensor exhibited stable and reversible photoswitching characteristics while maintaining the original current output. After being compressed by 50%, the current output was slightly reduced but still had the photoswitching characteristics (Fig. 7e–g). Furthermore, the image sensor enabled retina-like imaging when conforming to a hemispherical support. Shen et al. [122] fabricated a flexible image sensor on a PET substrate for broadband detection. This device consists of 10 × 10 pixels, in which each pixel consists of SnS QDs/Zn<sub>2</sub>SnO<sub>4</sub> nanowires and two interdigital electrodes (Fig. 7h, i). Zn<sub>2</sub>SnO<sub>4</sub> nanowires have a bandgap of about 3.6 eV, which is widely used in UV image sensors. To expand the spectral response range, the authors chose SnS QDs with a narrow bandgap of ~ 1.3 eV as a sensitizer. The spectral response test indicated that the device had a broadband photoresponse from UV to NIR. The mechanical stability of the image sensor was verified by bending tests. The current values remained constant as the bending angle  $\theta$  increased from 0° to 150° and then recovered to 0° (Fig. 7j). After 5000 bending cycles, the responsivity of the flexible image sensor can maintain 95% of the initial value, indicating excellent folding endurance. Meanwhile, the flexible image sensor under a bending state achieved the recognition of a target image composed of white light and red light, indicating excellent target recognition ability (Fig. 7k, l).

### 3.1.5 Hemispherical designs

Traditional imaging systems rely on planar image sensors, such as CMOS image sensors and charge-coupled devices (CCD). These systems typically require large and complex multi-lens optics to mitigate optical aberrations for clear imaging. In contrast, hemispherical image sensors offer the advantage of simplifying lens designs by adapting their curvature to align with the focal plane, enabling wide-field-of-view imaging [18]. Nevertheless, the construction of hemispherical image sensors presents a significant challenge, since mainstream microfabrication processes are typically performed on flat surfaces.

A common approach to fabricating hemispherical image sensors involves initially preparing them using traditional lithography and then transferring them onto curved surfaces. Various techniques are employed to create

hemispherical devices, which include ultra-thin designs, origami structures, island-bridge structures, and combinations of these approaches. Bao et al. reported an ultrathin hemispherical image sensor array with photo-memory transistors (Fig. 8a, b) [123]. The fabrication process of this device involved the preparation of an ultrathin transistor array by conventional photolithography followed by transferring to a hemispherical surface (Fig. 8c). The SiN<sub>x</sub> layer at the bottom of the device was a rigid island to prevent buckling in those regions. After the transferring, the designed rigid island structures were aligned with the transistor channel region, resulting in compression buckling occurred only in the interconnect region. Owing to the hemispherical focal plane structure, the image sensor realized imaging only with the aid of a simple concentric lens. In addition, after the image was exposed, the image sensor successfully can reconstruct the original image even if the light source was removed during subsequent reading. Kim et al. reported a hemispherical image sensor array by using a strain-releasing device structure and atomically thin MoS<sub>2</sub>-graphene heterostructures (Fig. 8d) [124]. The phototransistor array was composed of a MoS<sub>2</sub>-graphene heterostructure (6 nm), Al<sub>2</sub>O<sub>3</sub> dielectric (25 nm), Ti/Au gate (5/10 nm), and Si<sub>3</sub>N<sub>4</sub> substrate (5 nm) (Fig. 8e). The entire thickness of the device is only 51 nm. Due to the ultrathin thickness and softness of the 2D material, the device exhibited much lower induced strain than the fracture strain of the constituent material. The truncated icosahedron and the stress-isolated island structure designs made the device fully attached to the hemispherical surface. The device successfully captured various images with the help of single-lens optics (Fig. 8f). Ma et al. [125] demonstrated an origami approach for a silicon-based hemispherical image sensor. In geometric mathematics, a quasi-spherical solid is made up of the truncated icosahedron, which is a combination of multiple pentagons and hexagonal faces. In this work, 676 polygonal blocks were mapped into a net of half-truncated icosahedrons and then folded to form a hemisphere (Fig. 8g). Before deforming, the entire device fabrication process, including silicon etching, metal deposition and device passivation, was completed using planar processing technologies. Leaving the deformation process to the last step ensured the viability of most semiconductor manufacturing techniques. Figure 8h displays a photograph of a folded truncated icosahedron, where metalized silicon nanomembrane blocks were printed on a flexible polyimide substrate. The device can be folded into concave or convex hemispheres (Fig. 8i, j). This hemispherical image sensor achieved high-resolution imaging through multiple imaging from different angles and reconstruction by computer software, demonstrating the potential application in hemispherical electronic eye systems.

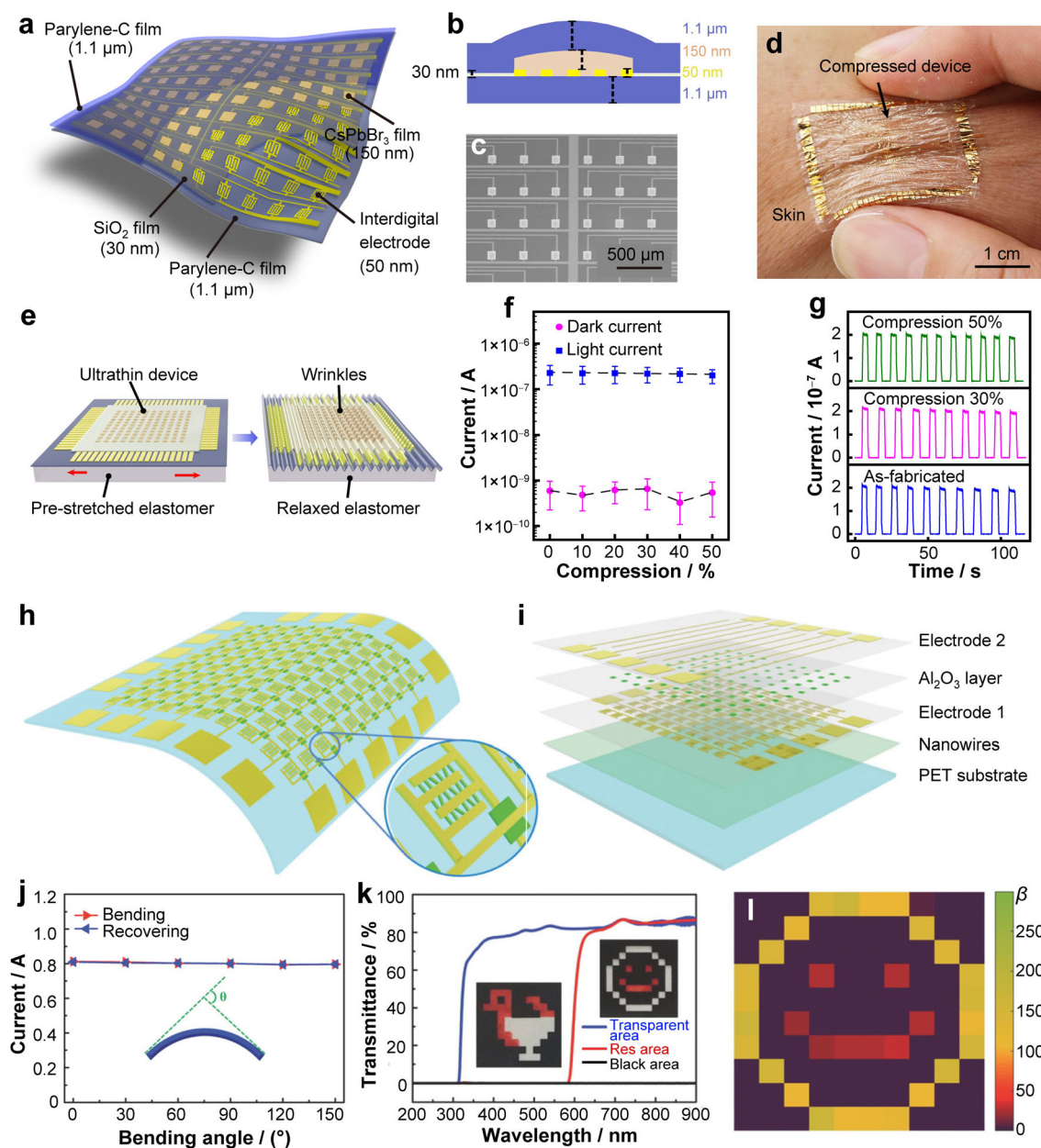


**Fig. 7** High flexible image sensors: **a, b** structural diagrams of a flexible perovskite image sensor. **c** SEM image of the active area of the device. **d** Photograph of flexible image sensor attached to the skin. **e** Schematic illustration of the mechanical stability test of the device under compression. **f, g** The current outputs and the photoswitching characteristic of the device under different compressive states. Reproduced with permission from Ref. [121]. Copyright 2021, Wiley–VCH. **h, i** Structural diagrams of a flexible broadband image sensor. **j** Current outputs of the device under different bending angles. **k** Transmittance spectra of the PET mask with different colors. **l** The corresponding imaging result of the flexible broadband image sensor. Reproduced with permission from Ref. [122]. Copyright 2018, Wiley–VCH

In 2019, Fan's group proposed another scheme to fabricate hemispherical image sensors by using the hemispherical template [126]. For preparing a hemispherical device, a porous aluminum oxide membrane (PAM) template was fabricated by deforming an aluminum sheet into a hemispherical shape and anodizing it. Perovskite nanowire arrays were grown in the PAM template by a vapor-

phase deposition process as photosensitive materials. A tungsten film on an aluminum hemispherical shell worked as a common electrode. By mimicking the vitreous humor in the human eye, ionic liquids were employed to ensure that the electrodes were fully in contact with the nanowires. The flexible eutectic gallium indium liquid metal wires worked as a discrete electrode to connect the nanowires to

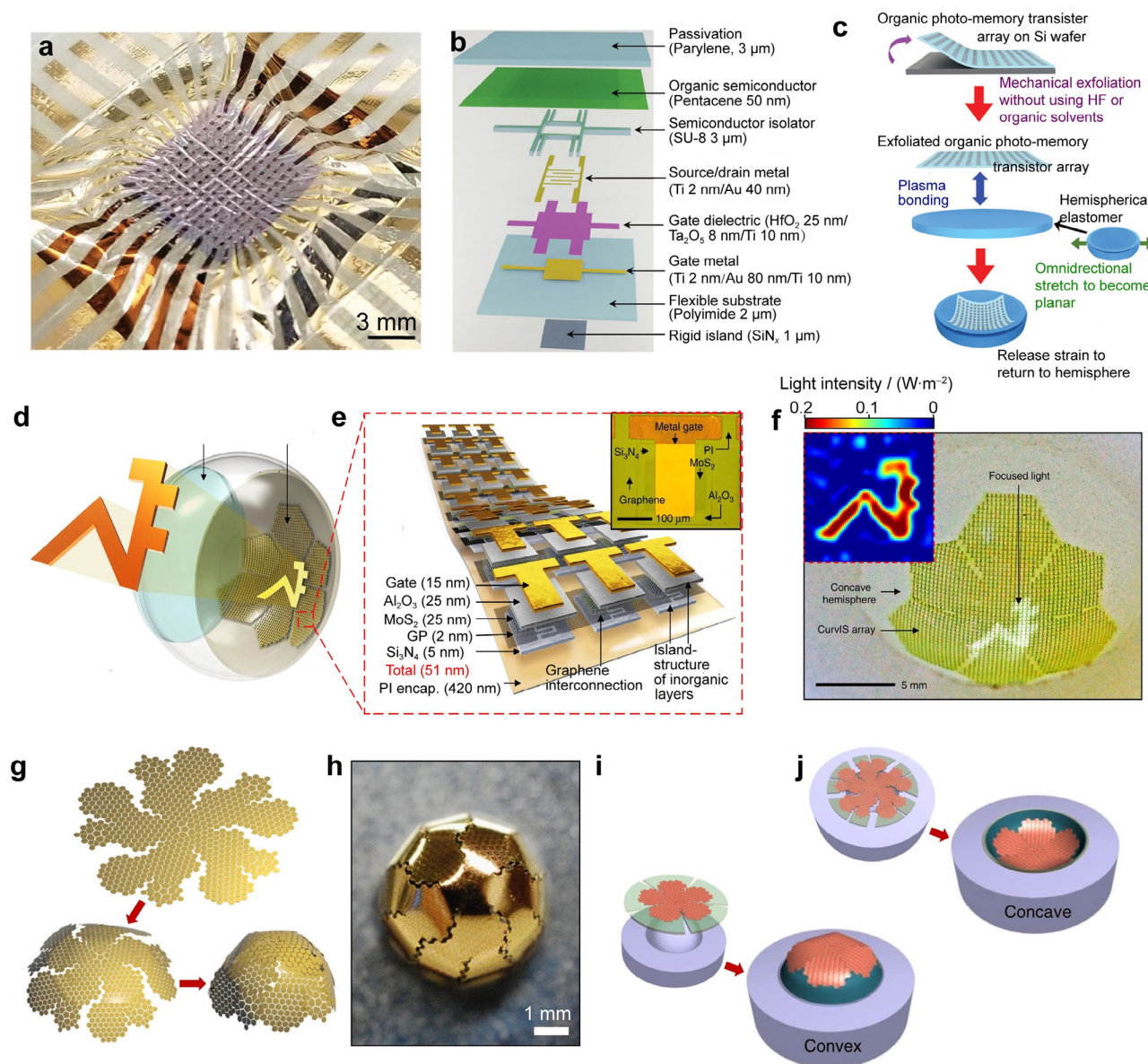


**Fig. 8** Hemispherical image sensors: **a** photograph of an ultrathin hemispherical image sensor array. **b** Schematic diagram of device hierarchical structure. **c** Schematic diagram of the device assembly process. Reproduced with permission from Ref. [123]. Copyright 2023, Wiley–VCH. **d, e** Structural diagrams of a hemispherical image sensor with the stress-isolated island structure. **f** Photograph of the hemispherical image sensor and the pattern imaged by the device. Reproduced with permission from Ref. [124]. Copyright 2017, Springer Nature. **g** Schematic illustration of the assembly of a hemispherical image sensor by an origami approach. **h** Photograph of the hemispherical image sensor with a folded truncated icosahedron. **i, j** The schematic demonstration of the device folded into concave or convex hemispheres. Reproduced with permission from Ref. [125]. Copyright 2017, Springer Nature

the external circuitry through the discontinuous indium adhesion layer. This image sensor realized the reconstruction of the optical pattern projected onto it. Compared to planar image sensors, this hemispherical image sensor has a more consistent distance between the pixels and the lens, resulting in better focus and a wide field of view. The hemispherical image sensor has a diagonal field of view of about  $100.1^\circ$ , which is much larger than a planar device with only  $69.8^\circ$ . In 2022, Fan et al. demonstrated a

hemispherical mid- to long-infrared image sensor by a similar method [127]. The structure diagram of the device is shown in Fig. 9a. The core components of this device are hemispherical PAM templates and semiconductor thermoelectric materials. Ionic thermoelectric polymer materials were filled into the template as an infrared absorption layer (Fig. 9b). At small temperature differences, the device exhibited ultra-high thermopower, as shown in Fig. 9c. Thus, this device presented excellent staring imaging

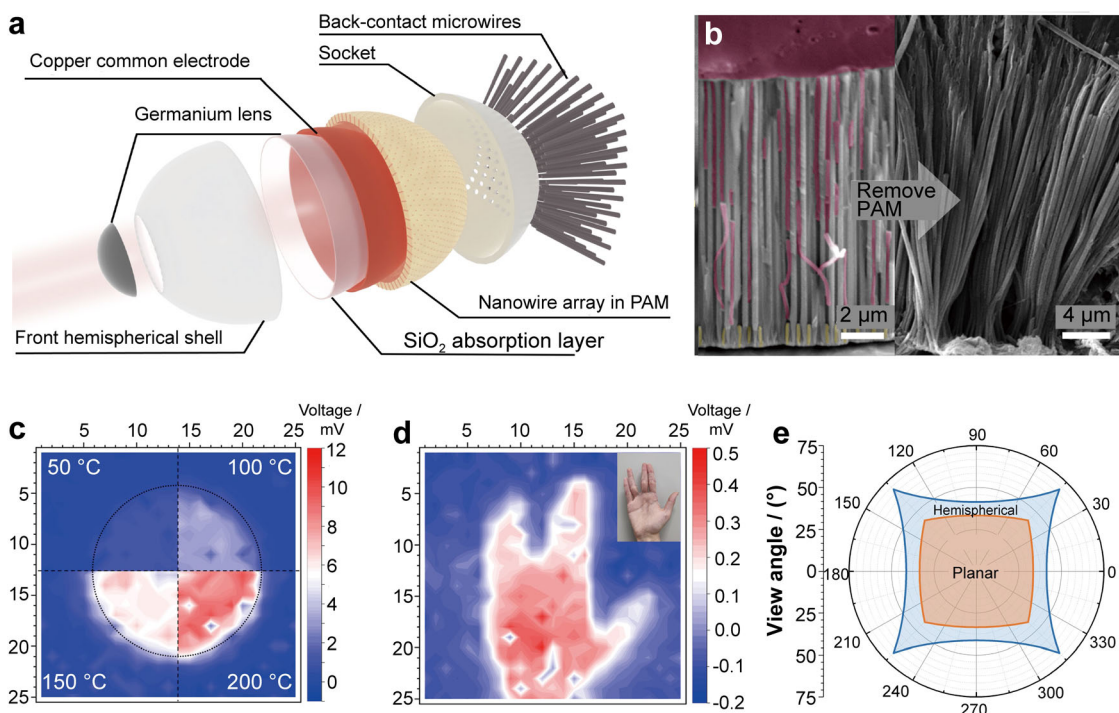


**Fig. 9** Hemispherical image sensors: **a** structural diagram of hemispherical perovskite image sensor fabricated by PAM template. **b** SEM images of ionic thermoelectric materials grown in the PAM template. **c** The images of the blackbody furnace at different temperatures captured by the device. **d** An image of the human hand at room temperature captured by the device. **e** Comparison of view angle for planar and hemispherical image sensors. Reproduced with permission from Ref. [127]. Copyright 2022, Amer Assoc Advancement Science

capabilities for human hand gestures and heated symbols ( $\sim 60\text{ }^{\circ}\text{C}$ ) (Fig. 9d). The hemispherical device structure endowed it with an ultrawide field of view of  $135^{\circ}$ , much larger than the field of view of the snake's pit organ with infrared imaging capabilities (Fig. 9e).

### 3.1.6 Self-power supply

Self-powered image sensors constitute a significant category of optoelectronic devices that operate independently of external power sources [128, 129]. Compared with traditional image sensors, self-powered image sensors are well-suited for addressing the imperative requirement for low power consumption in future imaging systems. The working principle of the self-powered image sensor is based on the photovoltaic effect, which can generate a built-in electric field. The built-in electric field acts as a driving force within the image sensor to separate the photogenerated electron-hole pairs without an external power supply [130]. The most common way to assemble self-powered image sensors relies on constructing heterojunctions, such as type-II heterojunctions, P-N junctions, P-I-N junctions and Schottky junctions.

Zhai et al. [131] fabricated a self-powered image sensor by Se/Si type-II heterojunction (Fig. 10a). According to the

optical band gap, electrons drifted from Si to Se after contact, forming a built-in electric field at the heterojunction interface (Fig. 10b). In this work, high-quality Se/Si interfaces were prepared by converting amorphous Se into crystalline Se in-situ by infrared radiation. Benefiting from the high-quality interface and appropriate energy band arrangement between Se and Si, the image sensor exhibited high detectivity ( $8.52 \times 10^{12}$  Jons) and fast response time (183/405  $\mu\text{s}$ ) in the self-powered mode. Furthermore, the self-powered image sensor exhibited stable photoswitching characteristics and realized imaging without bias voltage (Fig. 10c). Jie et al. assembled a self-powered UV image sensor based on the p-GeSe<sub>2</sub>/n-GaN junction (Fig. 10d) [132]. Considering the band configuration, when GeSe<sub>2</sub> and GaN were irradiated by photons with energy greater than their band gaps, the electrons and holes moved towards n-GaN and p-GeSe<sub>2</sub> respectively under the action of the built-in electric field, generating photocurrent at a bias voltage of 0 V (Fig. 10e). The device exhibited excellent photoresponse in both UV and Vis spectral regions, and the UV-Vis rejection ratio can be as high as  $1.8 \times 10^5$  (Fig. 10f). The successful preparation of wafer-scale GeSe<sub>2</sub> films on GaN substrate made it possible to assemble self-powered image sensor arrays. As a proof of concept, a  $4 \times 4$  array device demonstrated UV imaging in

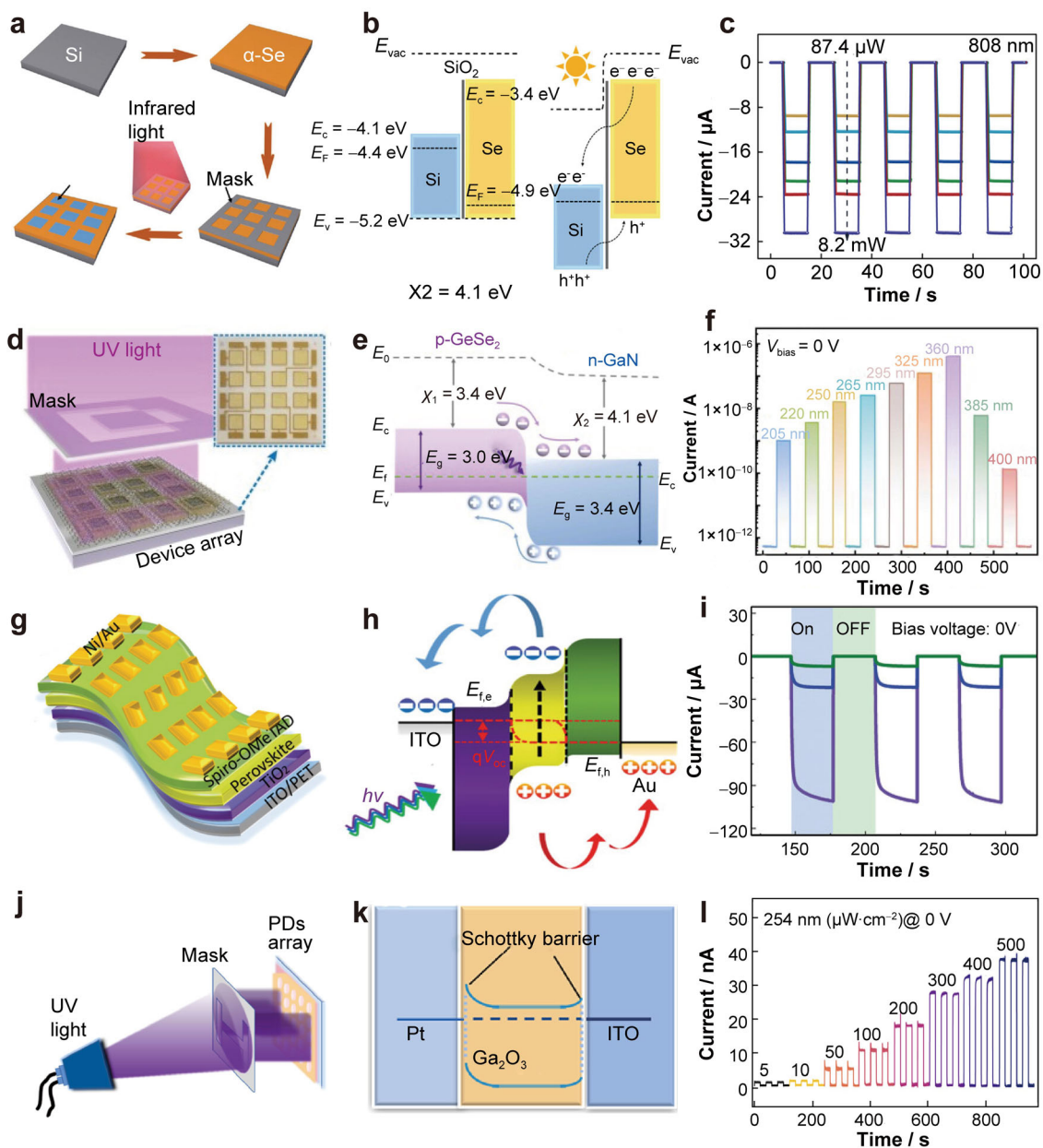


**Fig. 10** Self-powered image sensors: **a–c** device structure, working principle, and photoswitching characteristic of the self-powered image sensor fabricated by Se/Si type-II heterojunction. Reproduced with permission from Ref. [131]. Copyright 2022, Wiley–VCH. **d–f** Device structure, working principle, and photoswitching characteristic of the self-powered image sensor fabricated by the p-GeSe<sub>2</sub>/n-GaN junction. Reproduced with permission from Ref. [132]. Copyright 2022, Elsevier. **g–i** Device structure, working principle, and photoswitching characteristic of the self-powered image sensor fabricated by the p-spiro-OMeTAD/i-CsPbBr<sub>3</sub>/n-TiO<sub>2</sub> junctions. Reproduced with permission from Ref. [57]. Copyright 2020, Wiley–VCH. **j–l** Device structure, working principle, and photoswitching characteristic of the self-powered image sensor fabricated by Pt/a-Ga<sub>2</sub>O<sub>3</sub>/ITO Schottky junction. Reproduced with permission from Ref. [133]. Copyright 2023, The Optical Society of America

self-powered mode. Wu et al. reported a self-powered flexible image sensor based on P-I-N junctions (Fig. 10g). The high-quality CsPbBr<sub>3</sub> QDs were synthesized as photosensitive material via the CsBr/KBr treatment. Spiro-OMeTAD and TiO<sub>2</sub> were used as p- and n-type conductive materials, respectively [57]. The operating principle of this device is shown in Fig. 10h. Under the irradiation of

visible light, electron–hole pairs were generated in the perovskite layer due to its inherent light absorption. The generated electrons and holes migrated in opposite directions, from CsPbBr<sub>3</sub> to TiO<sub>2</sub> and CsPbBr<sub>3</sub> to spiro-OMeTAD, and were finally collected by ITO and Ni/Au, respectively. In the self-powered mode, the device exhibited a stable photoresponse at different wavelengths of light

(Fig. 10i). All pixels of the device showed a uniform photoresponse, presenting potential applications in image sensing. Ye et al. [133] reported a self-powered solar-blind image sensor by utilizing Pt/a-Ga<sub>2</sub>O<sub>3</sub>/ITO vertical Schottky junction (Fig. 10j). When  $\alpha$ -Ga<sub>2</sub>O<sub>3</sub> was in contact with Pt and ITO respectively, the Fermi levels between them aligned towards the same plane due to the flow of electrons, resulting in asymmetric back-to-back Schottky junctions at the Pt/a-Ga<sub>2</sub>O<sub>3</sub> and a-Ga<sub>2</sub>O<sub>3</sub>/ITO interfaces (Fig. 10k). Eventually, two built-in electric fields with opposite directions were generated. Since, the Schottky junction at the Pt/ $\alpha$ -Ga<sub>2</sub>O<sub>3</sub> interface was significantly stronger than that at the  $\alpha$ -Ga<sub>2</sub>O<sub>3</sub>/ITO interface, the net built-in electric field of this device was mainly controlled by the Schottky junction at the Pt/ $\alpha$ -Ga<sub>2</sub>O<sub>3</sub> interface. The photocurrent of the device under 254 nm light illumination increased with the light intensity at a bias voltage of 0 V (Fig. 10l). The Schottky junction image sensor was proved to have excellent deep UV imaging capability without the power supply.

## 3.2 Neuromorphic vision sensors

Neuromorphic vision sensors enable advanced image acquisition and data processing superior to conventional frame-based image sensors [134, 135]. The function of neuromorphic vision sensors is gradually approaching that of biological vision systems. This section mainly introduces the significant achievements of neuromorphic vision sensors in neuromorphic imaging and data processing, environment adaptation, and ultra-low power consumption.

### 3.2.1 Neuromorphic imaging and data processing

In the human vision system, image recognition needs to undergo the following processes [136]. (1) Optical signals emitted or reflected from an external object enter the human eyes and are imaged on the retina. (2) Image information is preprocessed in the retina. (3) Optic nerve fibers transmit action potentials to the brain. (4) Image information is further processed by synapses in neural networks to realize recognition and memory. According to the characteristics of each part of the above processes, a variety of bionic neuromorphic vision sensors have been developed.

In an endeavor that emulates the detection capabilities of the retina and the memory function of the brain, Shen and colleagues introduced an artificial visual memory system by employing UV-stimulated memristors (Fig. 11a–c) [137]. The memristor consisted of an In<sub>2</sub>O<sub>3</sub>-based image sensor and an Al<sub>2</sub>O<sub>3</sub>-based memristor in series. When the image sensor was irradiated by UV light, the memristor changed from the HRS to the LRS, realizing the

memory of UV information (Fig. 11d). Under the action of reverse voltage, the memristor recovered from the LRS to the HRS, erasing the optical information. As an artificial vision system, the array devices achieved UV imaging and memorizing functions (Fig. 11e, f). Compared with the conventional image sensor, this device adds the information memory function. Inspired by the retinal preprocessing function, Zhou et al. [75] demonstrated a neuromorphic vision sensor based on ORRAM. The ORRAM with a structure of Pd/MoO<sub>x</sub>/ITO exhibited light-dependent synaptic plasticity and nonvolatile memory function. Meanwhile, the ORRAM achieved image preprocessing, including contrast enhancement and noise reduction, increasing the efficiency and accuracy of subsequent image recognition. The simulation results showed that without ORRAM preprocessing, the recognition rate was low and reached 0.980 after 2000 training epochs, while with ORRAM preprocessing, the recognition rate reached 0.986 after only 1000 training epochs. Mimicking the curved structure and information preprocessing capacity of the retina, Kim et al. demonstrated curved neuromorphic vision sensors based on a heterostructure of MoS<sub>2</sub> and poly(1,3,5-trimethyl-1,3,5-trivinyl cyclotrisiloxane) (Fig. 11g, h) [11]. Derived from charge trapping in the interface between heterojunctions, this device presented light-triggered synaptic plasticity and memory behavior (Fig. 11i). As a curved imaging system, the curved neuromorphic vision sensor achieved neuromorphic imaging from noisy light input with the aid of a plano-convex lens (Fig. 11j, k). Furthermore, the pre-processed images were memorized and slowly dissipated, which is similar to the behavior of biological memory. Beyond conventional image contour recognition, Parkd et al. demonstrated optic-neural synapse (ONS) as neuromorphic vision sensors for color-mixed pattern recognition (Fig. 11l) [138]. The ONS device consisted of an optical-sensing unit and a synaptic unit. The whole device was integrated on the same h-BN/WSe<sub>2</sub> heterojunction, where the synaptic device was specially designed with a weight control layer on h-BN by the oxygen plasma treatment process (Fig. 11m). The devices showed different synaptic behaviors when triggered by different wavelengths of light. By combining device performance parameters with an optic-neural network (ONN), the recognition tasks of color patterns or mixed-color patterns were successfully realized (Fig. 11n). This research lays a foundation for building neural networks with the function of color pattern recognition.

### 3.2.2 Environmental adaptation

One of the notable features of the human visual system is that photoreceptors containing rod and cone cells in the retina can adapt to the external light environment and

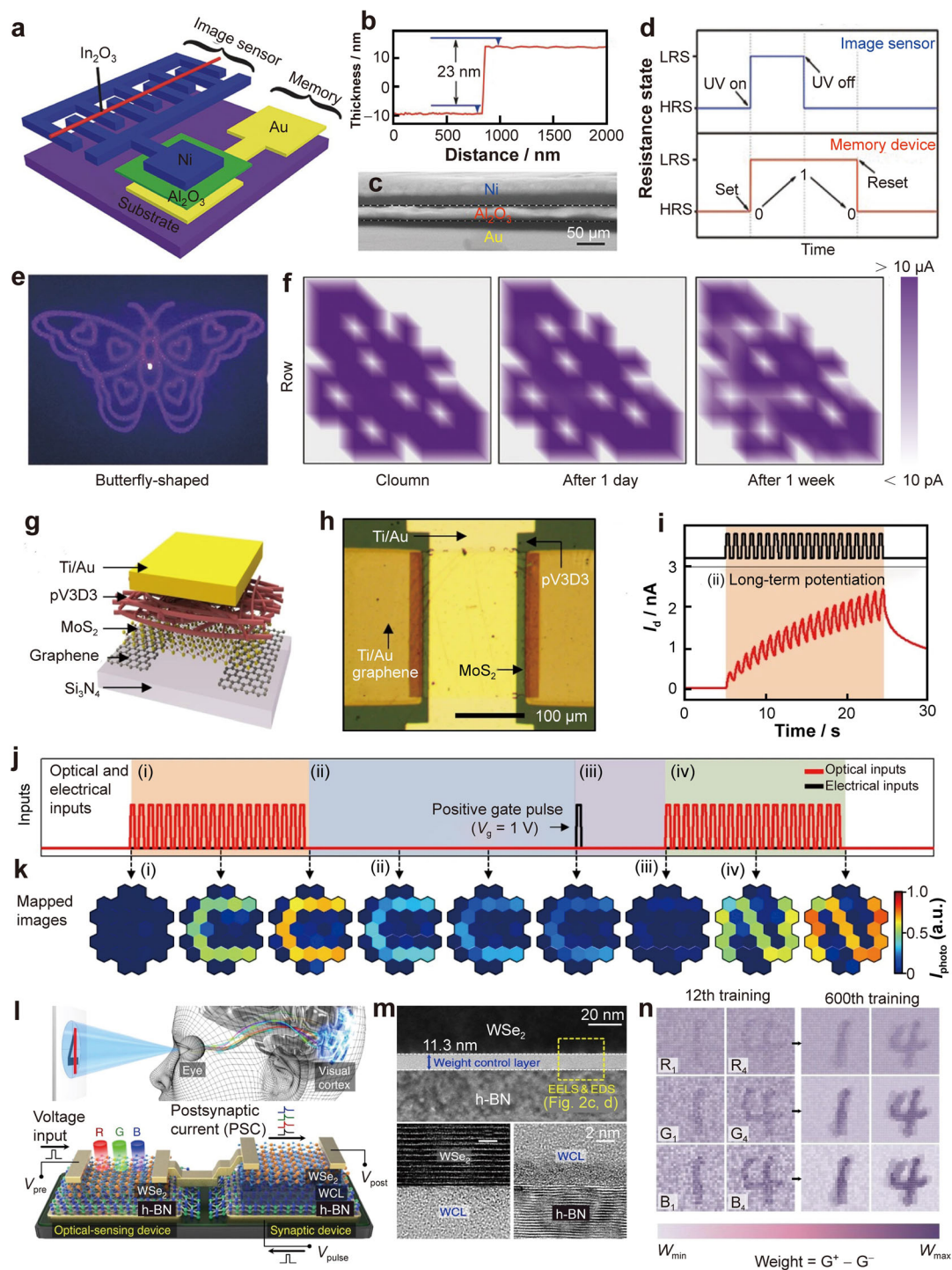


**Fig. 11** Neuromorphic vision sensors with the capacity of imaging and data processing: **a** structural diagram of an artificial visual memory system based on memristors and image sensors. **b** The thickness of  $\text{Al}_2\text{O}_3$  film in memristor. **c** Cross-section SEM image of the memristor. **d** The changes of resistance states of a memristor with motivated by an image sensor. **e**, **f** Original optical pattern and the corresponding images memorized by the systems. Reproduced with permission from Ref. [137]. Copyright 2018, Wiley-VCH. **g** Structural diagram of curved neuromorphic vision sensors based on  $\text{MoS}_2$  and pV3D3. **h** Microscopical optical image of the device. **i** Synaptic behavior of devices stimulated by optical signals. **j**, **k** The optical and electrical signals and the corresponding recognized images of neuromorphic vision sensors at different times. Reproduced with permission from Ref. [11]. Copyright 2022, Springer Nature. **l** Structural diagram of neuromorphic vision sensors for color-mixed pattern recognition. **m** Cross-section of SEM and TEM images of the device. **n** Image recognition situations undergo different training through algorithms. Reproduced with permission from Ref. [138]. Copyright 2018, Springer Nature

produce the appropriate level of electrical spikes depending on the light intensity. There are two cases of biological visual adaptation: scotopic and photopic adaptation [139]. Mimicking biological visual adaptations to build environment-adaptable neuromorphic vision sensors can make them have more accurate imaging ability in tanglesome light environments.

In pioneer reports, such devices were prepared by logically integrating multiple electronic components. Park et al. demonstrated an environment-adaptable neuromorphic vision sensor by integrating a photovoltaic divider and an ionotronic synaptic transistor (Fig. 12a) [140]. The photovoltaic divider consisted of a visible light-sensitive CdSe photodetector and a visible-light-blind IGZO transistor, in which the IGZO transistor acted as a load transistor. The ionotronic synaptic transistor was constructed by employing a solid electrolyte of Na-doped  $\text{Al}_2\text{O}_3$  as the gate dielectric layer and IGZO films as the channel material. By adjusting the resistance ratio of the photodetector and the load transistor, the photovoltaic divider provided properly distributed electrical spikes for the gate of the ionotronic synaptic transistor (Fig. 12b). This device successfully demonstrated synaptic plasticity (Fig. 12c). More importantly, this device realized visual adaptation (photopic and scotopic adaptation) by modulating the load gate bias. In a bright light environment, image recognition is required to increase the load gate bias, while faint images in a dark environment can be recognized by reducing the load gate bias (Fig. 12d, e). This work opens a precedent for building environment-adaptable neuromorphic vision sensors. Through a similar strategy, Seong et al. [141] also fabricated an environment-adaptable neuromorphic vision sensor. The structural improvement is that a solid-electrolyte-based indium-zinc-oxide load neurotransistor was used to replace the IGZO load transistor. The advantage in terms of performance is the implementation of habitual visual processing by the introduction of a pulsed load bias, enabling more accurate image preprocessing and spontaneous recovery.

Owing to the complexity of the structure, the existing environment-adaptable devices based on logic circuits are not conducive to large-scale integration. To address this challenge, the gate bias-assisted trapping/de-trapping mechanism has been introduced into environment-adaptable neuromorphic vision sensors. The introduction of defect states in the environment-adaptable devices endows it with a non-constant current output under a certain light intensity. Chai et al. [142] reported an environment-adaptable neuromorphic vision sensor based on bottom-gated  $\text{MoS}_2$  phototransistors. The charge trap states were intentionally imported at the interface of  $\text{MoS}_2$  films through ultraviolet/ozone treatment. The defect state can trap or de-trap electrons at different gate voltages, allowing the

conductance of the device to be dynamically modulated and providing scotopic and photopic adaptation. When positive bias was applied, the photocurrent of  $\text{MoS}_2$  phototransistors decreased under repeated strong light stimulation due to the continuous trapping of photogenerated electrons by the interface defect states. This made the device insensitive and suitable for bright image recognition. In contrast, when the reverse bias was applied, the photoresponse of the device was particularly sensitive and suitable for recognizing dark images, due to the stable generation of photogenerated carriers under the stimulus of weak light input without defect trapping. Cao et al. [76] demonstrated an InP QDs/InSnZnO neuromorphic vision sensor with environment-adaptive capacity (Fig. 12f). Oxygen vacancy defects in InSnZnO films were utilized to achieve electron trapping and de-trapping under bias modulation. In the forward bias, a great deal of electrons were injected into the InSnZnO channel, obtaining high photocurrent, while the electrons were trapped simultaneously and the electrostatic field repelled the injection of electrons, causing photocurrent to decrease over time (Fig. 12g). Conversely, the electrons were de-trapped when a reverse bias was applied. The negative gate bias depleted the free carriers, resulting in an ultra-low dark current, and the photogenerated carriers continued to increase in dark environments (Fig. 12h). Based on the above principle, this device realized image recognition in bright and dim environments under forward and reverse bias respectively, demonstrating excellent environment-adaptive capacity (Fig. 12i, j).

### 3.2.3 Ultra-low power consumption

Biological synapses have information processing capacity with low power consumption. For example, the human brain possessing  $10^{11}$  neurons and  $10^{15}$  synapses is known as the most efficient processor with each synaptic event consuming only  $\sim 1$ –100 fJ [143, 144]. Currently, some neuromorphic vision sensors have low-power consumption characteristics, which are comparable to biological synapses. Huang et al. [73] reported broadband neuromorphic vision sensors with ultralow power consumption based on PbS QDs/Pentacene heterostructure (Fig. 13a). The device achieved an ultra-low power consumption of 0.55 fJ per spike at a low operating voltage of  $-0.01$  V (Fig. 13b). Zhang et al. [145] demonstrated organic field-effect transistors as ultra-low power neuromorphic vision sensors (Fig. 13c). This device successfully simulated the response of visual nerves to external light stimuli with an energy consumption of 0.07–34 fJ per synaptic event for short-term plasticity and 0.41–19.87 fJ per synaptic event for long-term plasticity, both of which are close to the energy efficiency of biological synapses (Fig. 13d). Hu et al. [146]

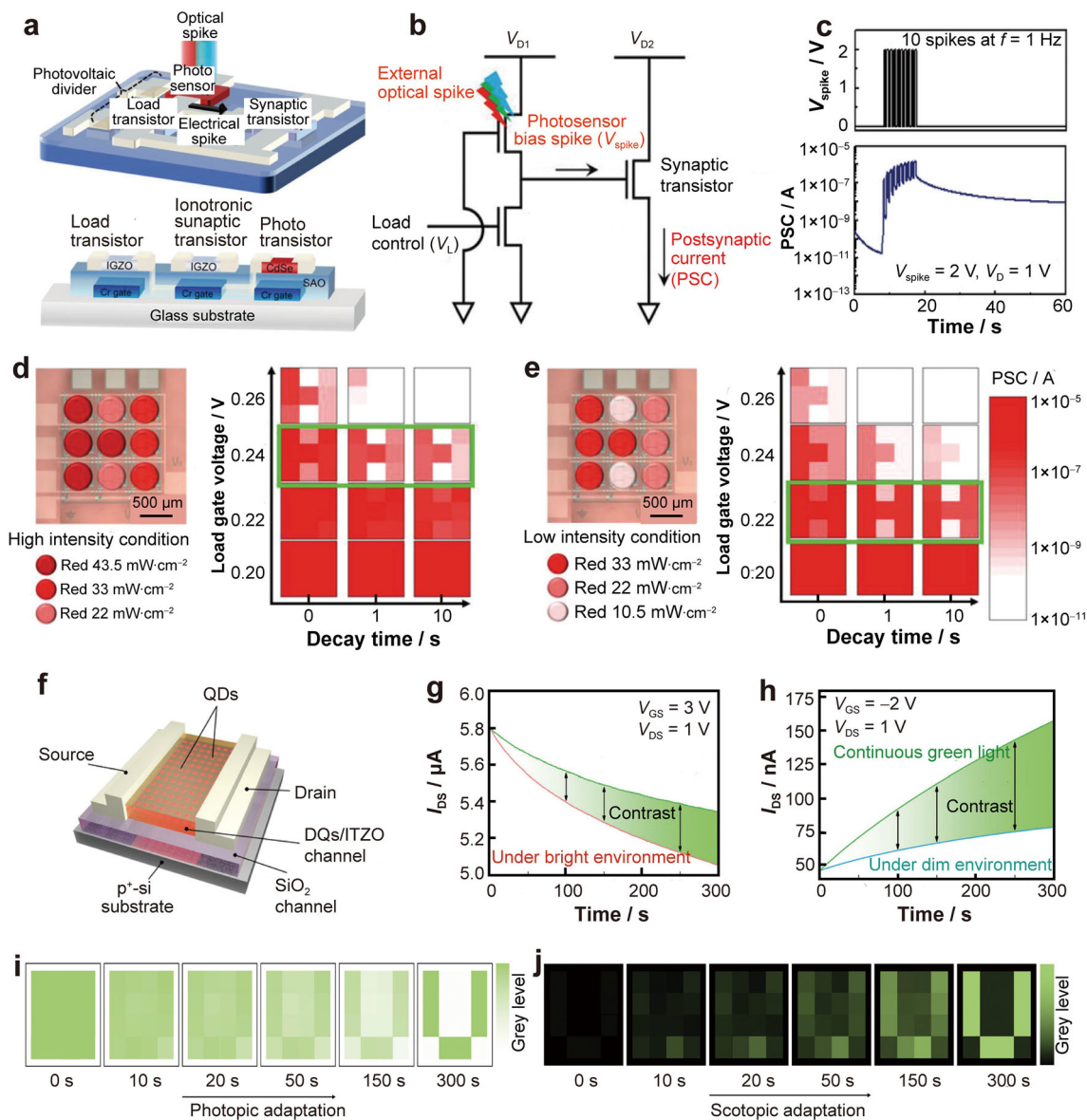


**Fig. 12** Environment-adaptable neuromorphic vision sensor: **a** structural diagram of an environment-adaptable neuromorphic vision sensor fabricated by integrating photovoltaic dividers and ionotronic synaptic transistors. **b** Equivalent circuit diagram of the device. **c** Synaptic behavior of devices stimulated by optical signals. **d, e** The recognized images of the device under high light intensity and low light intensity conditions. Reproduced with permission from Ref. [140]. Copyright 2019, Wiley–VCH. **f** Structural diagram of an environment-adaptable neuromorphic vision sensor based on gate bias-assisted trapping/de-trapping mechanism. **g, h** Under different gate biases, the photocurrent of the device changes with time under bright light and dim light environments. **i, j** The photopic adaptation and scotopic adaptation behaviors of the devices in different light environments. Reproduced with permission from Ref. [76]. Copyright 2023, Wiley–VCH

assembled an ultra-low power neuromorphic vision sensor based on MoS<sub>2</sub> layers by indium (In)-induced surface charge doping (Fig. 13e). The introduction of In layer enhanced the conductivity of the MoS<sub>2</sub> channel and effectively reduced the power consumption of the synaptic device. The power consumption per synaptic event of this device was reduced from 71.69 fJ to 68.9 aJ, which is much lower than the power consumption of biological synapses (Fig. 13f). In addition, a novel device structure

with photovoltaic effects allow photonic synaptic devices to operate without a power supply. Han et al. reported a self-powered neuromorphic vision sensor based on photovoltaic devices and memristive arrays (Fig. 13g) [147]. When stimulated by external light, the solar cell generated presynaptic signals, and the perovskite-based memristor conducted further information preprocessing (Fig. 13h). The experimental results proved that the neuromorphic

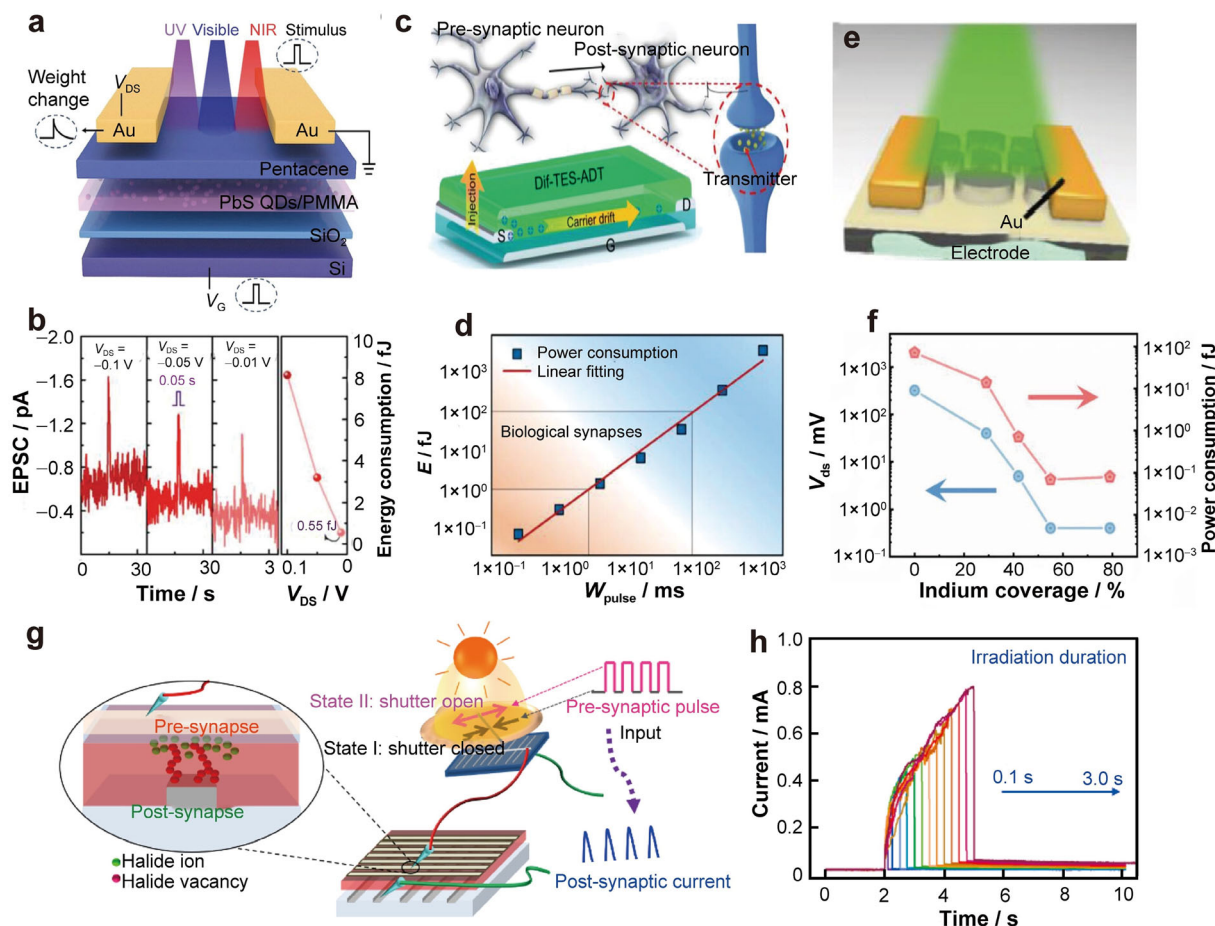


**Fig. 13** Ultra-low power neuromorphic vision sensors: **a** structural diagram of the ultra-low power broadband neuromorphic vision sensor. **b** Synaptic current and the corresponding power consumption of the device under different bias voltages. Reproduced with permission from Ref. [73]. Copyright 2023, Wiley–VCH. **c** Structural diagram of the ultra-low power organic FETs neuromorphic vision sensor. **d** The power consumption per spike of this device under different pulse widths. Reproduced with permission from Ref. [145]. Copyright 2022, Wiley–VCH. **e** Structural diagram of ultra-low power neuromorphic vision sensor based on In-doping MoS<sub>2</sub> films. **f** The variation of power consumption of synaptic devices as a function of the In coverage. Reproduced with permission from Ref. [146]. Copyright 2021, Wiley–VCH. **g**, **h** Structural diagram and the synaptic behaviors of the self-powered neuromorphic vision sensor based on photovoltaic devices and memristive arrays. Reproduced with permission from Ref. [147]. Copyright 2020, Elsevier

vision sensor without a power supply achieved clear image perception by contrast enhancement and noise reduction.

#### 4 Conclusions and perspectives

As a crucial module in image recognition systems, imaging devices are undergoing rapid development. In this review, we provide an overview of state-of-the-art image sensors and neuromorphic vision sensors. Conventional image sensors have made great improvements in device structure, working mechanisms and functionalities. Neuromorphic vision sensors not only exhibit basic synaptic behaviors but also advanced neuronal functions such as image recognition and adaptability to light environmental conditions. However, it is essential to acknowledge that both image

sensors and neuromorphic vision sensors have their imperfections.

- (1) The stability of imaging devices in the atmospheric environment should be paid enough attention. Instabilities often arise from photosensitive materials, which are highly sensitive to oxygen or moisture in the atmospheric environment. For instance, the unpackaged organic–inorganic hybrid perovskite-based image sensors experience significant performance degradation within a short time in the atmospheric environment. Similarly, neuromorphic vision sensors based on metal oxide films are susceptible to oxygen in the atmospheric environment. Enhancing the stability of imaging devices requires the development of effective packaging techniques or

improvements in the inherent stability of photosensitive materials.

- (2) The evolution of flexible imaging devices has expanded their applications and enhanced user comfort, particularly in wearable products. Nevertheless, signal readout in flexible imaging devices encounters significant challenges. Presently, signal reading is predominantly carried out through rigid Si-based readout circuits. When it is applied to flexible image sensors, the connection between these rigid circuits and the flexible image sensor meets considerable difficulties. The exploitation of flexible readout circuits and the innovations in interconnection technology are essential. In recent years, emerging liquid metals may offer a solution for building fully flexible systems.
- (3) There is an ongoing trade-off between achieving high-resolution and large-scale assembly due to limitations posed by semiconductor materials or device assembly technologies. In this regard, the fabrication of conventional image sensors is more mature than neuromorphic vision sensors. CMOS integrated circuits have made significant contributions to the construction of large-scale and high-resolution image sensors. However, the current neuromorphic vision sensors are only integrated on a small scale. To overcome this limitation, on the one hand, large-scale semiconductor material synthesis technology should be explored, and on the other hand, traditional CMOS technology can also be applied to the construction of large-scale and high-resolution neuromorphic vision sensors.
- (4) The application of neuromorphic vision sensors holds the promise of simplifying the structure and enhancing the efficiency of image recognition systems. Although the synaptic behaviors of neuromorphic vision sensors have been studied extensively, the actual implementation of neuromorphic networks has been rarely reported. This bottleneck arises from a limited understanding of the intricate relationship between synaptic structure and function. Moreover, the working principle of current synaptic devices differs from biological synapses and it may not fully meet the demands of implementing neural networks. Solving this challenge necessitates interdisciplinary collaboration involving experts in materials, physics, electronics, neuroscience and other fields.
- (5) Neuromorphic vision sensors hold potential applications in the development of artificial eyeballs. Although various types of neuromorphic vision sensors have been developed, biocompatible devices are still rarely reported. Therefore, greater attention should be given to the biocompatibility of such

devices. Directly using biocompatible materials to build devices, or using biocompatible materials to encapsulate existing devices are effective ways to build biocompatible neuromorphic vision sensors.

**Acknowledgements** This study was financially supported by the National Natural Science Foundation of China (Nos. 52202181, 52125205, U20A20166, 52192614, 52372154, 52002246 and U22A2077), the National Key R&D Program of China (Nos. 2021YFB3200302 and 2021YFB3200304), the Natural Science Foundation of Beijing Municipality (Nos. Z180011 and 2222088), China Postdoctoral Science Foundation (No. 2022M712166), Shenzhen Science and Technology Program (No. KQTD20170810105439418) and the Fundamental Research Funds for the Central Universities.

#### Declarations

**Conflict of interests** Cao-Feng Pan is an editorial board for *Rare Metals* and was not involved in the editorial review or the decision to publish this article. All authors declare that there are no competing interests.

#### References

- [1] Chen YC, Lu YJ, Liao MY, Tian YZ, Liu Q, Gao CJ, Yang X, Shan CX. 3D solar-blind Ga<sub>2</sub>O<sub>3</sub> photodetector array realized via origami method. *Adv Funct Mater.* 2019;29(50):1906040. <https://doi.org/10.1002/adfm.201906040>.
- [2] Ni S, Liu Y, Tong S, Li S, Song X. Emerging NIR-II luminescent gold nanoclusters for in vivo bioimaging. *J Anal Test.* 2023;7(3):260. <https://doi.org/10.1007/s41664-023-00256-0>.
- [3] Zheng JX, Zhou ZA, Feng T, Li H, Sun CH, Wang N, Tian Y, Zhao Y, Zhou SY. Hydrophobic long-chain two-dimensional perovskite scintillators for underwater X-ray imaging. *Rare Met.* 2023. <https://doi.org/10.1007/s12598-023-02421-x>.
- [4] Wang CF, Dong L, Peng DF, Pan CF. Tactile sensors for advanced intelligent systems. *Adv Intell Syst.* 2019;1(8):1900090. <https://doi.org/10.1002/aisy.201900090>.
- [5] Hou B, Zhang CP, Yang SB. Computer vision tool-setting system of numerical control machine tool. *Sensors.* 2020;20(18):5302. <https://doi.org/10.3390/s20185302>.
- [6] Qureshi F, Terzopoulos D. Smart camera networks in virtual reality. *Proc IEEE.* 2008;96(10):1640. <https://doi.org/10.1109/jproc.2008.928932>.
- [7] Oike Y. Evolution of image sensor architectures with stacked device technologies. *IEEE Trans Electron Devices.* 2022;69(6):2757. <https://doi.org/10.1109/ted.2021.3097983>.
- [8] Xia KL, Wu WQ, Zhu MJ, Shen XY, Yin Z, Wang HM, Li S, Zhang MC, Wang HM, Lu HJ, Pan AL, Pan CF, Zhang YY. CVD growth of perovskite/graphene films for high-performance flexible image sensor. *Sci Bull.* 2020;65(5):343. <https://doi.org/10.1016/j.scib.2019.12.015>.
- [9] Cho SW, Jo C, Kim YH, Park SK. Progress of materials and devices for neuromorphic vision sensors. *Nano-Micro Lett.* 2022;14(1):203. <https://doi.org/10.1007/s40820-022-00945-y>.
- [10] Zhu QB, Li B, Yang DD, Liu C, Feng S, Chen ML, Sun Y, Tian YN, Su X, Wang XM, Qiu S, Li QW, Li XM, Zeng HB, Cheng HM, Sun DM. A flexible ultrasensitive optoelectronic sensor array for neuromorphic vision systems. *Nat Commun.*



- 2021;12(1):1798. <https://doi.org/10.1038/s41467-021-22047-w>.
- [11] Choi C, Leem J, Kim M, Taqieddin A, Cho C, Cho KW, Lee GJ, Seung H, Bae HJ, Song YM, Hyeon T, Aluru NR, Nam S, Kim DH. Curved neuromorphic image sensor array using a MoS<sub>2</sub>-organic heterostructure inspired by the human visual recognition system. *Nat Commun*. 2022;13(1):5141. <https://doi.org/10.1038/s41467-022-32731-0>.
- [12] Ansari S, Bianconi S, Kang CM, Mohseni H. From material to cameras: low-dimensional photodetector arrays on CMOS. *Small Methods*. 2023. <https://doi.org/10.1002/smt.202300595>.
- [13] Cheng ZZ, Zhao T, Zeng HB. 2D material-based photodetectors for infrared imaging. *Small Sci*. 2022;2(1):2100051. <https://doi.org/10.1002/sm.202100051>.
- [14] Yokota T, Fukuda K, Someya T. Recent progress of flexible image sensors for biomedical applications. *Adv Mater*. 2021; 33(19):2004416. <https://doi.org/10.1002/adma.202004416>.
- [15] Zhao N, Qiao S, Ma W, Xu LL, Hao XL, Huang QH. Research progress on performance and application of pyroelectric materials. *Chin J Rare Met*. 2022;46(9):1225. <https://doi.org/10.13373/j.cnki.cjrm.XY22060026>.
- [16] Bao RR, Tao J, Pan CF, Wang ZL. Piezophototronic effect in nanosensors. *Small Sci*. 2021;1(6):2000060. <https://doi.org/10.1002/sm.202000060>.
- [17] Wang ZN, Yu RM, Pan CF, Liu Y, Ding Y, Wang ZL. Piezo-phototronic UV/Visible photosensing with optical-fiber-nanowire hybridized structures. *Adv Mater*. 2015; 27(9):1553. <https://doi.org/10.1002/adma.201405274>.
- [18] Gao WC, Xu ZS, Han X, Pan CF. Recent advances in curved image sensor arrays for bioinspired vision system. *Nano Today*. 2022;42: 101366. <https://doi.org/10.1016/j.nantod.2021.101366>.
- [19] Zuber F, Chambion B, Gaschet C, Caplet S, Nicolas S, Charrière S, Henry D. Tolerancing and characterization of curved image sensor systems. *Appl Opt*. 2020;59(28):8814. <https://doi.org/10.1364/ao.400950>.
- [20] Park J, Chong J. Pattern transformation method for digital camera with Bayer-like white-RGB color filter array. *IEICE Trans Inf Syst*. 2015;E98D(11):2021. <https://doi.org/10.1587/transinf.2014EDL8249>.
- [21] Xue J, Zhu ZF, Xu XB, Gu Y, Wang SL, Xu LM, Zou YS, Song JZ, Zeng HB, Chen Q. Narrowband perovskite photodetector-based image array for potential application in artificial vision. *Nano Lett*. 2018;18(12):7628. <https://doi.org/10.1021/acs.nanolett.8b03209>.
- [22] Han ZY, Liao XF, Zou YS, He Y, Li JY, Gu Y, Hu DW, Liu JX, Zuo LJ, Liu YS, Xu XB. Flexible miniaturized multi-spectral detector derived from blade-coated organic narrow-band response unit array. *ACS Nano*. 2022;16(12):21036. <https://doi.org/10.1021/acsnano.2c08731>.
- [23] Lou Z, Shen GZ. Flexible image sensors with semiconducting nanowires for biomimic visual applications. *Small Struct*. 2021;2(7):2000152. <https://doi.org/10.1002/sstr.202000152>.
- [24] Deng W, Zhang XJ, Huang LM, Xu XZ, Wang L, Wang JC, Shang QX, Lee ST, Jie JS. Aligned single-crystalline perovskite microwire arrays for high-performance flexible image sensors with long-term stability. *Adv Mater*. 2016;28(11):2201. <https://doi.org/10.1002/adma.201505126>.
- [25] Knipp D, Street RA, Stiebig H, Krause M, Lu JP, Ready S, Ho J. Vertically integrated thin film color sensor arrays for imaging applications. *Opt Express*. 2006;14(8):3106. <https://doi.org/10.1364/oe.14.003106>.
- [26] Liu K, Wang XY, Su HS, Chen XY, Wang D, Guo J, Shao L, Bao WZ, Chen HL. Large-scale MoS<sub>2</sub> pixel array for imaging sensor. *Nanomaterials*. 2022;12(23):4118. <https://doi.org/10.3390/nano12234118>.
- [27] Xu XY, Jin XM. Integrated photonic computing beyond the von neumann architecture. *ACS Photonics*. 2023;10(4):1027. <https://doi.org/10.1021/acsp Photonics.2c01543>.
- [28] Bian JH, Cao ZY, Zhou P. Neuromorphic computing: devices, hardware, and system application facilitated by two-dimensional materials. *Appl Phys Rev*. 2021;8(4):041313. <https://doi.org/10.1063/5.0067352>.
- [29] Wu NJ. Neuromorphic vision chips. *Sci China Inf Sci*. 2018; 61(6):060421. <https://doi.org/10.1007/s11432-017-9303-0>.
- [30] Demir HS, Christen JB, Ozev S. Energy-efficient image recognition system for marine life. *IEEE Trans Comput-Aided Des Integr Circuits Syst*. 2020;39(11):3458. <https://doi.org/10.1109/tcad.2020.3012745>.
- [31] Palmerston JB, Zhou YR, Chan RHM. Comparing biological and artificial vision systems: network measures of functional connectivity. *Neurosci Lett*. 2020;739:135407. <https://doi.org/10.1016/j.neulet.2020.135407>.
- [32] Hong XT, Huang YL, Tian QL, Zhang S, Liu C, Wang LM, Zhang K, Sun J, Liao L, Zou XM. Two-dimensional perovskite-gated AlGaIn/GaN high-electron-mobility-transistor for neuromorphic vision sensor. *Adv Sci*. 2022;9(27):2202019. <https://doi.org/10.1002/advs.202202019>.
- [33] Kim MS, Kim MS, Lee GJ, Sunwoo SH, Chang S, Song YM, Kim DH. Bio-inspired artificial vision and neuromorphic image processing devices. *Adv Mater Technol*. 2022;7(2):2100144. <https://doi.org/10.1002/admt.202100144>.
- [34] Du JY, Xie DG, Zhang QH, Zhong H, Meng FQ, Fu XK, Sun QC, Ni H, Li T, Guo EJ, Guo HZ, He M, Wang C, Gu L, Xu XL, Zhang GY, Yang GZ, Jin KJ, Ge C. A robust neuromorphic vision sensor with optical control of ferroelectric switching. *Nano Energy*. 2021;89:106439. <https://doi.org/10.1016/j.nanoen.2021.106439>.
- [35] Pan X, Jin TY, Gao J, Han C, Shi YM, Chen W. Stimuli-enabled artificial synapses for neuromorphic perception: progress and perspectives. *Small*. 2020;16(34):2001504. <https://doi.org/10.1002/smll.202001504>.
- [36] Xie DD, Wei LB, Xie M, Jiang LY, Yang JL, He J, Jiang J. Photoelectric visual adaptation based on 0D-CsPbBr<sub>3</sub>-quantum-dots/2D MoS<sub>2</sub> mixed-dimensional heterojunction transistor. *Adv Funct Mater*. 2021;31(14):2010655. <https://doi.org/10.1002/adfm.202010655>.
- [37] Park HL, Kim H, Lim D, Zhou H, Kim YH, Lee Y, Park S, Lee TW. Retina-inspired carbon nitride-based photonic synapses for selective detection of UV light. *Adv Mater*. 2020;32(11):1906899. <https://doi.org/10.1002/adma.201906899>.
- [38] Jiang T, Wang Y, Zheng YS, Wang L, He X, Li LQ, Deng YF, Dong H, Tian HK, Geng YH, Xie LH, Lei Y, Ling HF, Ji DY, Hu W. Tetrachromatic vision-inspired neuromorphic sensors with ultraweak ultraviolet detection. *Nat Commun*. 2023;14(1):2281. <https://doi.org/10.1038/s41467-023-37973-0>.
- [39] Li ZQ, Yan TT, Fang XS. Low-dimensional wide-bandgap semiconductors for UV photodetectors. *Nat Rev Mater*. 2023; 8(9):587. <https://doi.org/10.1038/s41578-023-00583-9>.
- [40] Li Y, Shi ZF, Li XJ, Shan CX. Photodetectors based on inorganic halide perovskites: materials and devices. *Chin Phys B*. 2019;28(1):017803. <https://doi.org/10.1088/1674-1056/28/1/017803>.
- [41] Wang H, Kim DH. Perovskite-based photodetectors: materials and devices. *Chem Soc Rev*. 2017;46(17):5204. <https://doi.org/10.1039/c6cs00896h>.
- [42] Lopes GRF, de Castro S, Kawata B, Rapp PHD, Abramof E, Peres ML. Photoconductivity effect in SnTe quantum well. *Appl Phys Lett*. 2021;119(3):032104. <https://doi.org/10.1063/5.0056230>.



- [43] Beattie AR, Cunningham RW. Large-signal photoconductive effect. *J Appl Phys.* 1964;35(2):353. <https://doi.org/10.1063/1.1713317>.
- [44] Zhang KX, Zhang LB, Han L, Wang L, Chen ZQ, Xing HZ, Chen XS. Recent progress and challenges based on two-dimensional material photodetectors. *Nano Express.* 2021;2(1):012001. <https://doi.org/10.1088/2632-959X/abd45b>.
- [45] He JJ, Chen KX, Huang CL, Wang XM, He YN, Dan YP. Explicit gain equations for single crystalline photoconductors. *ACS Nano.* 2020;14(3):3405. <https://doi.org/10.1021/acsnano.9b09406>.
- [46] Lee Y, Cha S, Kim C. Bandwidth enhancement of graphene-organic hybrid photoconductors by accelerating electron transfer processes at graphene interface. *Adv Mater Interfaces.* 2021;8(15):2100478. <https://doi.org/10.1002/admi.202100478>.
- [47] Lu XC, Lu YZ, Wang C, Cao Y. Efficient photoelectrodes based on two-dimensional transition metal dichalcogenides heterostructures: from design to construction. *Rare Met.* 2022;41(4):1142. <https://doi.org/10.1007/s12598-021-01875-1>.
- [48] De Iacovo A, Venettacci C, Giansante C, Colace L. Narrowband colloidal quantum dot photodetectors for wavelength measurement applications. *Nanoscale.* 2020;12(18):10044. <https://doi.org/10.1039/d0nr02626c>.
- [49] Li F, Wang XD, Xia ZG, Pan CF, Liu QL. Photoluminescence tuning in stretchable PDMS film grafted doped core/multishell quantum dots for anticounterfeiting. *Adv Funct Mater.* 2017;27(17):1700051. <https://doi.org/10.1002/adfm.201700051>.
- [50] An S, Huang YC, Wu CY, Huang PR, Chang GE, Lai JY, Seo JH, Kim M. Single-crystalline Ge<sub>1-x</sub>Sn<sub>x</sub>/Si p-n heterojunction photodiodes with Sn compositions up to 10%. *Adv Mater Technol.* 2023;8(4):2201136. <https://doi.org/10.1002/admt.202201136>.
- [51] Zhang YW, Ma KK, Zhao C, Hong W, Nie CJ, Qiu ZJ, Wang S. An ultrafast WSe<sub>2</sub> photodiode based on a lateral pin homojunction. *ACS Nano.* 2021;15(3):4405. <https://doi.org/10.1021/acsnano.0c08075>.
- [52] Sturman B, Podivilov E. Tip-enhanced bulk photovoltaic effect. *Phys Rev B.* 2017;96(13):134107. <https://doi.org/10.1103/PhysRevB.96.134107>.
- [53] Zou HY, Dai GZ, Wang AC, Li XG, Zhang SL, Ding WB, Zhang L, Zhang Y, Wang ZL. Alternating current photovoltaic effect. *Adv Mater.* 2020;32(11):1907249. <https://doi.org/10.1002/adma.201907249>.
- [54] Hu X, Li XY, Li GY, Ji T, Ai FJ, Wu JH, Ha E, Hu JQ. Recent progress of methods to enhance photovoltaic effect for self-powered heterojunction photodetectors and their applications in inorganic low-dimensional structures. *Adv Funct Mater.* 2021;31(24):2011284. <https://doi.org/10.1002/adfm.202011284>.
- [55] Chai Y. Silicon photodiodes that multiply. *Nat Electron.* 2022;5(8):483. <https://doi.org/10.1038/s41928-022-00822-x>.
- [56] Lim Y, Yun S, Minami D, Choi T, Choi H, Shin J, Park S, Heo CJ, Leem DS, Yagi T, Park KB, Kim S. Green-light-selective organic photodiodes with high detectivity for CMOS color image sensors. *ACS Appl Mater.* 2021;13(8):10664. <https://doi.org/10.1021/acsaami.1c01930>.
- [57] Shen K, Xu H, Li X, Guo J, Sathasivam S, Wang MQ, Ren AB, Choy KL, Parkin IP, Guo ZX, Wu J. Flexible and self-powered photodetector arrays based on all-inorganic CsPbBr<sub>3</sub> quantum dots. *Adv Mater.* 2020;32(22):2000004. <https://doi.org/10.1002/adma.202000004>.
- [58] Peng DF, Liu XH, Pan CF. Epitaxial lift-off for controllable single-crystalline perovskites. *Sci Bull.* 2021;66(1):6. <https://doi.org/10.1016/j.scib.2020.09.002>.
- [59] Liu XQ, Yang XN, Gao GY, Yang ZY, Liu HT, Li Q, Lou Z, Shen GZ, Liao L, Pan CF, Wang ZL. Enhancing photoresponsivity of self-aligned MoS<sub>2</sub> field-effect transistors by piezo-phototronic effect from GaN nanowires. *ACS Nano.* 2016;10(8):7451. <https://doi.org/10.1021/acsnano.6b01839>.
- [60] Wei SL, Wang F, Zou XM, Wang LM, Liu C, Liu XQ, Hu WD, Fan ZY, Ho JC, Liao L. Flexible quasi-2D perovskite/IGZO phototransistors for ultrasensitive and broadband photodetection. *Adv Mater.* 2020;32(6):1907527. <https://doi.org/10.1002/adma.201907527>.
- [61] Hong S, Zagni N, Choo S, Liu N, Baek S, Bala A, Yoo H, Kang BH, Kim HJ, Yun HJ, Alam MA, Kim S. Highly sensitive active pixel image sensor array driven by large-area bilayer MoS<sub>2</sub> transistor circuitry. *Nat Commun.* 2021;12(1):3559. <https://doi.org/10.1038/s41467-021-23711-x>.
- [62] Wu WQ, Wang XD, Han X, Yang Z, Gao GY, Zhang YF, Hu JF, Tan YW, Pan AL, Pan CF. Flexible photodetector arrays based on patterned CH<sub>3</sub>NH<sub>3</sub>PbI<sub>3-x</sub>Cl<sub>x</sub> perovskite film for real-time photosensing and imaging. *Adv Mater.* 2019;31(3):1805913. <https://doi.org/10.1002/adma.201805913>.
- [63] Zhang YQ, Ma Y, Wang YX, Zhang XD, Zuo CT, Shen L, Ding LM. Lead-free perovskite photodetectors: progress, challenges, and opportunities. *Adv Mater.* 2021;33(26):2006691. <https://doi.org/10.1002/adma.202006691>.
- [64] Shen L, Fang YJ, Wei HT, Yuan YB, Huang JS. A highly sensitive narrowband nanocomposite photodetector with gain. *Adv Mater.* 2016;28(10):2043. <https://doi.org/10.1002/adma.201503774>.
- [65] Furlan F, Nodari D, Palladino E, Angela E, Mohan L, Briscoe J, Fuchter MJ, Macdonald TJ, Grancini G, McLachlan MA, Gasparini N. Tuning halide composition allows low dark current perovskite photodetectors with high specific detectivity. *Adv Opt Mater.* 2022;10(24):2201816. <https://doi.org/10.1002/adom.202201816>.
- [66] Dou LT, Yang Y, You JB, Hong ZR, Chang WH, Li G, Yang Y. Solution-processed hybrid perovskite photodetectors with high detectivity. *Nat Commun.* 2014;5:5404. <https://doi.org/10.1038/ncomms6404>.
- [67] Dong KL, Zhou H, Xiao M, Gui PB, Gao Z, Yao F, Shao WL, Liu CW, Tao C, Ke WJ, Fang GJ. Semi-transparent, high-performance lead-free Cs<sub>3</sub>Bi<sub>2</sub>I<sub>9</sub> single crystal self-driven photodetector. *Appl Phys Lett.* 2022;120(19):191102. <https://doi.org/10.1063/5.0090569>.
- [68] Liu CL, Wang L, Chen XS, Politano A, Wei DC, Chen G, Tang WW, Lu W, Tredicucci A. Room-temperature high-gain long-wavelength photodetector via optical-electrical controlling of hot carriers in graphene. *Adv Opt Mater.* 2018;6(24):1800836. <https://doi.org/10.1002/adom.201800836>.
- [69] Liu L, Cheng ZQ, Jiang B, Liu YX, Zhang YL, Yang F, Wang JH, Yu XF, Chu PK, Ye C. Optoelectronic artificial synapses based on two-dimensional transitional-metal trichalcogenide. *ACS Appl Mater.* 2021;13(26):30797. <https://doi.org/10.1021/acsaami.1c03202>.
- [70] Yao P, Wu HQ, Gao B, Eryilmaz SB, Huang XY, Zhang WQ, Zhang QT, Deng N, Shi LP, Wong HSP, Qian H. Face classification using electronic synapses. *Nat Commun.* 2017;8:15199. <https://doi.org/10.1038/ncomms15199>.
- [71] Cheng ZG, Ríos C, Pernice WHP, Wright CD, Bhaskaran H. On-chip photonic synapse. *Sci Adv.* 2017;3(9): e1700160. <https://doi.org/10.1126/sciadv.1700160>.
- [72] Jiang S, Nie S, He Y, Liu R, Chen C, Wan Q. Emerging synaptic devices: from two-terminal memristors to multiterminal neuromorphic transistors. *Mater Today Nano.* 2019;8:100059. <https://doi.org/10.1016/j.mtnano.2019.100059>.
- [73] Zhang JY, Guo P, Guo ZY, Li L, Sun TR, Liu DP, Tian L, Zu GQ, Xiong LZ, Zhang JH, Huang J. Retina-inspired artificial

- synapses with ultraviolet to near-infrared broadband responses for energy-efficient neuromorphic visual systems. *Adv Funct Mater.* 2023;33(32):2302885. <https://doi.org/10.1002/adfm.202302885>.
- [74] Jo C, Kim J, Kwak JY, Kwon SM, Park JB, Kim J, Park GS, Kim MG, Kim YH, Park SK. Retina-inspired color-cognitive learning via chromatically controllable mixed quantum dot synaptic transistor arrays. *Adv Mater.* 2022;34(12):2108979. <https://doi.org/10.1002/adma.202108979>.
- [75] Zhou FC, Zhou Z, Chen JW, Choy TH, Wang JL, Zhang N, Lin ZY, Yu SM, Kang JF, Wong HSP, Chai Y. Optoelectronic resistive random access memory for neuromorphic vision sensors. *Nat Nanotechnol.* 2019;14(8):776. <https://doi.org/10.1038/s41565-019-0501-3>.
- [76] Gao ZX, Ju X, Zhang HZ, Liu XH, Chen HY, Li WF, Zhang HL, Liang LY, Cao HT. InP quantum dots tailored oxide thin film phototransistor for bioinspired visual adaptation. *Adv Funct Mater.* 2023;33(52):2305959. <https://doi.org/10.1002/adfm.202305959>.
- [77] Wang HL, Zhao Q, Ni ZJ, Li QY, Liu HT, Yang YC, Wang LF, Ran Y, Guo YL, Hu WP, Liu YQ. A ferroelectric/electrochemical modulated organic synapse for ultraflexible, artificial visual-perception system. *Adv Mater.* 2018;30(46):1803961. <https://doi.org/10.1002/adma.201803961>.
- [78] Cohen-Cory S. The developing synapse: construction and modulation of synaptic structures and circuits. *Science.* 2002;298(5594):770. <https://doi.org/10.1126/science.1075510>.
- [79] Zhang Q, Jin TY, Ye X, Geng DC, Chen W, Hu WP. Organic field effect transistor-based photonic synapses: materials, devices, and applications. *Adv Funct Mater.* 2021;31(49):2106151. <https://doi.org/10.1002/adfm.202106151>.
- [80] Han X, Xu ZS, Wu WQ, Liu XH, Yan PG, Pan CF. Recent progress in optoelectronic synapses for artificial visual-perception system. *Small Struct.* 2020;1(3):2000029. <https://doi.org/10.1002/sstr.202000029>.
- [81] He YL, Zhu L, Zhu Y, Chen CS, Jiang SS, Liu R, Shi Y, Wan Q. Recent progress on emerging transistor-based neuromorphic devices. *Adv Intell Syst.* 2021;3(7):2000210. <https://doi.org/10.1002/aisy.202000210>.
- [82] Kullmann DM, Lamsa KP. Long-term synaptic plasticity in hippocampal interneurons. *Nat Rev Neurosci.* 2007;8(9):687. <https://doi.org/10.1038/nrn2207>.
- [83] Bliss TVP, Collingridge GL. A synaptic model of memory: long-term potentiation in the hippocampus. *Nature.* 1993;361(6407):31. <https://doi.org/10.1038/361031a0>.
- [84] Kim D, Lee JS. Neurotransmitter-induced excitatory and inhibitory functions in artificial synapses. *Adv Funct Mater.* 2022;32(21):2200497. <https://doi.org/10.1002/adfm.202200497>.
- [85] Ge SP, Huang FC, He JQ, Xu ZS, Sun ZH, Han X, Wang CF, Huang LB, Pan CF. Bidirectional photoresponse in perovskite-zno heterostructure for fully optical-controlled artificial synapse. *Adv Opt Mater.* 2022;10(11):2200409. <https://doi.org/10.1002/adom.202200409>.
- [86] Hu SG, Liu Y, Chen TP, Liu Z, Yu Q, Deng LJ, Yin Y, Hosaka S. Emulating the paired-pulse facilitation of a biological synapse with a NiOx-based memristor. *Appl Phys Lett.* 2013;102(18):183510. <https://doi.org/10.1063/1.4804374>.
- [87] Zhu R, Hang HL, Hu SG, Wang Y, Mei ZX. Amorphous-Ga<sub>2</sub>O<sub>3</sub> optoelectronic synapses with ultra-low energy consumption. *Adv Electron Mater.* 2022;8(1):2100741. <https://doi.org/10.1002/aelm.202100741>.
- [88] Wu WQ, Lu H, Han X, Wang CF, Xu ZS, Han ST, Pan CF. Recent progress on wavelength-selective perovskite photodetectors for image sensing. *Small Methods.* 2023;7(4):2201499. <https://doi.org/10.1002/smt.202201499>.
- [89] Jiang HL, Pan J, Zhou W, Li HM, Liu S. Fabrication and application of arrays related to two-dimensional materials. *Rare Met.* 2022;41(1):262. <https://doi.org/10.1007/s12598-021-01842-w>.
- [90] Wu WQ, Zhou MM, Li D, Li SM, Yang Z, Huo ZH, Wu YQ, Tan YW, Han X, Pan CF, Pan AN. A novel visible light sensing and recording system enabled by integration of photodetector and electrochromic devices. *Nanoscale.* 2021;13(20):9177. <https://doi.org/10.1039/d1nr01805a>.
- [91] Yang Z, Lu JF, ZhuGe MH, Cheng Y, Hu JF, Li FT, Qiao S, Zhang YF, Hu GF, Yang Q, Peng DF, Liu KH, Pan CF. Controllable growth of aligned monocrystalline CsPbB<sub>3</sub> microwire arrays for piezoelectric-induced dynamic modulation of single-mode lasing. *Adv Mater.* 2019;31(18):1900647. <https://doi.org/10.1002/adma.201900647>.
- [92] Liu JH, Zhang ZC, Qiao S, Fu GS, Wang SF, Pan CF. Lateral bipolar photoresistance effect in the CIGS heterojunction and its application in position sensitive detector and memory device. *Sci Bull.* 2020;65(6):477. <https://doi.org/10.1016/j.scib.2019.11.016>.
- [93] Chen MX, Pan CF, Zhang TP, Li XY, Liang RR, Wang ZL. Tuning light emission of a pressure-sensitive Silicon/ZnO nanowires heterostructure matrix through piezo-photonic effects. *ACS Nano.* 2016;10(6):6074. <https://doi.org/10.1021/acsnano.6b01666>.
- [94] Liang YG, Lu QC, Wu WQ, Xu ZS, Lu H, He ZP, Zhu YZ, Yu Y, Han X, Pan CF. A universal fabrication strategy for high-resolution perovskite-based photodetector arrays. *Small Methods.* 2023;7(9):2300339. <https://doi.org/10.1002/smt.202300339>.
- [95] Da Ponte RM, Gaio N, van Zeijl H, Vollebregt S, Dijkstra P, Dekker R, Serdijn WA, Giagka V. Monolithic integration of a smart temperature sensor on a modular silicon-based organ-on-a-chip device. *Sens Actuator A Phys.* 2021;317:112439. <https://doi.org/10.1016/j.sna.2020.112439>.
- [96] Jiang CM, Song JH. An ultrahigh-resolution digital image sensor with pixel size of 50 nm by vertical nanorod arrays. *Adv Mater.* 2015;27(30):4454. <https://doi.org/10.1002/adma.201502079>.
- [97] Tordera D, Peeters B, Akkerman HB, van Breemen A, Maas J, Shanmugam S, Kronemeijer AJ, Gelinck GH. A high-resolution thin-film fingerprint sensor using a printed organic photodetector. *Adv Mater Technol.* 2019;4(11):1900651. <https://doi.org/10.1002/admt.201900651>.
- [98] Deumel S, van Breemen A, Gelinck G, Peeters B, Maas J, Verbeek R, Shanmugam S, Akkerman H, Meulenkamp E, Huedler JE, Acharya M, García-Battle M, Almora O, Guerrero A, Garcia-Belmonte G, Heiss W, Schmidt O, Tedde SF. High-sensitivity high-resolution X-ray imaging with soft-sintered metal halide perovskites. *Nat Electron.* 2021;4(9):681. <https://doi.org/10.1038/s41928-021-00644-3>.
- [99] Kim J, Kwon SM, Kang YK, Kim YH, Lee MJ, Han K, Facchetti A, Kim MG, Park SK. A skin-like two-dimensionally pixelized full-color quantum dot photodetector. *Sci Adv.* 2019;5(11):eaax8801. <https://doi.org/10.1126/sciadv.aax8801>.
- [100] Kim J, Jo C, Kim MG, Park GS, Marks TJ, Facchetti A, Park SK. Vertically stacked full-color quantum dots phototransistor arrays for high-resolution and enhanced color-selective imaging. *Adv Mater.* 2022;34(2):2106215. <https://doi.org/10.1002/adma.202106215>.
- [101] Li KH, Lu Y, Yang XK, Fu LC, He JG, Lin XT, Zheng JJ, Lu SC, Chen C, Tang J. Filter-free self-power CdSe/Sb<sub>2</sub>(S<sub>1-x</sub>, Se<sub>x</sub>)<sub>3</sub> near-infrared narrowband detection and imaging. *Info-Mat.* 2021;3(10):1145. <https://doi.org/10.1002/inf.2.12237>.
- [102] Hou YC, Li JD, Yoon J, Knoepfel AM, Yang D, Zheng LY, Ye T, Ghosh S, Priya S, Wang K. Retina-inspired narrowband



- perovskite sensor array for panchromatic imaging. *Sci Adv.* 2023;9(15):eade2338. <https://doi.org/10.1126/sciadv.ade2338>.
- [103] Shevchenko A, Rousseau M, Friberg AT, Setälä T. Polarization time of unpolarized light. *Optica.* 2017;4(1):64. <https://doi.org/10.1364/optica.4.000064>.
- [104] Li SX, An Y, Sun XC, Zhu H, Xia H, Sun HB. Highly aligned organic microwire crystal arrays for high-performance polarization-sensitive photodetectors and image sensors. *Sci China Mater.* 2022;65(11):3105. <https://doi.org/10.1007/s40843-022-2079-3>.
- [105] Kong Z, Yin ZP, Cheng Y, Li YC, Zhang Z, Mei L. Modeling and evaluation of the systematic errors for the polarization-sensitive imaging lidar technique. *Remote Sens.* 2020;12(20):3309. <https://doi.org/10.3390/rs12203309>.
- [106] Altaqui A, Sen P, Schrickx H, Rech J, Lee JW, Escuti M, You W, Kim BJ, Kolbas R, O'Connor BT, Kudenov M. Mantis shrimp-inspired organic photodetector for simultaneous hyperspectral and polarimetric imaging. *Sci Adv.* 2021;7(10):eabe3196. <https://doi.org/10.1126/sciadv.abe3196>.
- [107] Song Q, Wang Y, Vogelbacher F, Zhan Y, Zhu DL, Lan YJ, Fang WZ, Zhang ZM, Jiang L, Song YL, Li MZ. Moire perovskite photodetector toward high-sensitive digital polarization imaging. *Adv Energy Mater.* 2021;11(29):2100742. <https://doi.org/10.1002/aenm.202100742>.
- [108] Wang J, Jiang CZ, Li WQ, Xiao XH. Anisotropic low-dimensional materials for polarization-sensitive photodetectors: from materials to devices. *Adv Opt Mater.* 2022;10(6):2102436. <https://doi.org/10.1002/adom.202102436>.
- [109] Yang YS, Liu SC, Wang X, Li ZB, Zhang Y, Zhang GM, Xue DJ, Hu JS. Polarization-sensitive ultraviolet photodetection of anisotropic 2D GeS<sub>2</sub>. *Adv Funct Mater.* 2019;29(16):1900411. <https://doi.org/10.1002/adfm.201900411>.
- [110] Venuthurumilli PK, Ye PD, Xu XF. Plasmonic resonance enhanced polarization-sensitive photodetection by black phosphorus in near infrared. *ACS Nano.* 2018;12(5):4861. <https://doi.org/10.1021/acsnano.8b01660>.
- [111] Ma WD, Lu JF, Wan BS, Peng DF, Xu Q, Hu GF, Peng YY, Pan CF, Wang ZL. Piezoelectricity in multilayer black phosphorus for piezotronics and nanogenerators. *Adv Mater.* 2020;32(7):1905795. <https://doi.org/10.1002/adma.201905795>.
- [112] Li L, Jin L, Zhou YX, Li JZ, Ma JQ, Wang S, Li WC, Li DH. Filterless polarization-sensitive 2D perovskite narrowband photodetectors. *Adv Opt Mater.* 2019;7(23):1900988. <https://doi.org/10.1002/adom.201900988>.
- [113] Yang H, Leow WR, Chen XD. 3D printing of flexible electronic devices. *Small Methods.* 2018;2(1):1700259. <https://doi.org/10.1002/smt.201700259>.
- [114] Li J, Yuan ZQ, Han X, Wang CF, Huo ZH, Lu QC, Xiong ML, Ma XL, Gao WC, Pan CF. Biologically inspired stretchable, multifunctional, and 3d electronic skin by strain visualization and triboelectric pressure sensing. *Small Sci.* 2022;2(1):2100083. <https://doi.org/10.1002/sssc.202100083>.
- [115] Chen ZB, Jin HH, Yang ZG, He DP. Recent advances on bioreceptors and metal nanomaterials-based electrochemical impedance spectroscopy biosensors. *Rare Met.* 2023;42(4):1098. <https://doi.org/10.1007/s12598-022-02129-4>.
- [116] Li HC, Jiang T, Zheng YS, Zou Y, Qi SL, Tian GF, Ji DY, Li LQ, Hu WP. Fluorinated dielectrics-modulated organic phototransistors and flexible image sensors. *Adv Opt Mater.* 2022;10(16):2200614. <https://doi.org/10.1002/adom.202200614>.
- [117] Li LD, Gu LL, Lou Z, Fan ZY, Shen GZ. ZnO quantum dot decorated Zn<sub>2</sub>SnO<sub>4</sub> nanowire heterojunction photodetectors with drastic performance enhancement and flexible ultraviolet image sensors. *ACS Nano.* 2017;11(4):4067. <https://doi.org/10.1021/acsnano.7b00749>.
- [118] Zuo SL, Chen P, Pan CF. Mechanism of magnetic field-modulated luminescence from lanthanide ions in inorganic crystal: a review. *Rare Met.* 2020;39(10):1113. <https://doi.org/10.1007/s12598-020-01450-0>.
- [119] Mo XM, Li T, Huang FC, Li ZX, Zhou YL, Lin T, Ouyang YF, Tao XM, Pan CF. Highly-efficient all-inorganic lead-free 1D CsCu<sub>2</sub>I<sub>3</sub> single crystal for white-light emitting diodes and UV photodetection. *Nano Energy.* 2021;81:105570. <https://doi.org/10.1016/j.nanoen.2020.105570>.
- [120] Hu JF, Chen G, Yu SZ, Lin YX, Wang KY, Li ZW, Zhang GD, Pan TF, Li YJ, Li MJ, Xia YD, Lv YF, Chen YH. Efficient micrometer-scale thick-film perovskite solar cells with superior stability. *Rare Met.* 2023. <https://doi.org/10.1007/s12598-023-02529-0>.
- [121] Wu WQ, Han X, Li J, Wang XD, Zhang YF, Huo ZH, Chen QS, Sun XD, Xu ZS, Tan YW, Pan CF, Pan AL. Ultrathin and conformable lead halide perovskite photodetector arrays for potential application in retina-like vision sensing. *Adv Mater.* 2021;33(9):2006006. <https://doi.org/10.1002/adma.202006006>.
- [122] Li LD, Lou Z, Shen GZ. Flexible broadband image sensors with SnS quantum dots/Zn<sub>2</sub>SnO<sub>4</sub> nanowires hybrid nanostructures. *Adv Funct Mater.* 2018;28(6):1705389. <https://doi.org/10.1002/adfm.201705389>.
- [123] Kim Y, Zhu C, Lee WY, Smith A, Ma H, Li X, Son D, Matsuhisa N, Kim J, Bae WG, Cho SH, Kim MG, Kurosawa T, Katsumata T, To JWF, Oh JY, Paik S, Kim SJ, Jin L, Yan F, Tok JBH, Bao Z. A hemispherical image sensor array fabricated with organic photomemory transistors. *Adv Mater.* 2023;35(1):2203541. <https://doi.org/10.1002/adma.202203541>.
- [124] Choi C, Choi MK, Liu SY, Kim MS, Park OK, Im C, Kim J, Qin XL, Lee GJ, Cho KW, Kim M, Joh E, Lee J, Son D, Kwon SH, Jeon NL, Song YM, Lu NS, Kim DH. Human eye-inspired soft optoelectronic device using high-density MoS<sub>2</sub>-graphene curved image sensor array. *Nat Commun.* 2017;8:1664. <https://doi.org/10.1038/s41467-017-01824-6>.
- [125] Zhang K, Jung YH, Mikael S, Seo JH, Kim M, Mi HY, Zhou H, Xia ZY, Zhou WD, Gong SQ, Ma ZQ. Origami silicon optoelectronics for hemispherical electronic eye systems. *Nat Commun.* 2017;8:1782. <https://doi.org/10.1038/s41467-017-01926-1>.
- [126] Gu LL, Poddar S, Lin YJ, Long ZH, Zhang DQ, Zhang QP, Shu L, Qiu X, Kam M, Javey A, Fan ZY. A biomimetic eye with a hemispherical perovskite nanowire array retina. *Nature.* 2020;581(7808):278. <https://doi.org/10.1038/s41586-020-2285-x>.
- [127] Ding YC, Liu GZ, Long ZH, Zhou Y, Qiu X, Ren BT, Zhang QP, Chi C, Wan ZA, Huang BL, Fan ZY. Uncooled self-powered hemispherical biomimetic pit organ for mid- to long-infrared imaging. *Sci Adv.* 2022;8(35):eaba8432. <https://doi.org/10.1126/sciadv.abq8432>.
- [128] Zhao Y, Gao WC, Dai K, Wang S, Yuan ZQ, Li JN, Zhai W, Zheng GQ, Pan CF, Liu CT, Shen CY. Bioinspired multifunctional photonic-electronic smart skin for ultrasensitive health monitoring, for visual and self-powered sensing. *Adv Mater.* 2021;33(45):2102332. <https://doi.org/10.1002/adma.202102332>.
- [129] Cong RD, Qiao S, Liu JH, Mi JS, Yu W, Liang BL, Fu GS, Pan CF, Wang SF. Ultrahigh, ultrafast, and self-powered visible-near-infrared optical position-sensitive detector based on a CVD-prepared vertically standing few-layer MoS<sub>2</sub>/Si heterojunction. *Adv Sci.* 2018;5(2):1700502. <https://doi.org/10.1002/advs.201700502>.
- [130] Tian W, Wang YD, Chen L, Li L. Self-powered nanoscale photodetectors. *Small.* 2017;13(45):1701848. <https://doi.org/10.1002/sml.201701848>.
- [131] Chang Y, Zhou YC, Wang JY, Zhai W. Constructing a high-quality t-Se/Si interface via in situ light annealing of a-Se for a self-powered image sensor. *Small.* 2022;18(25):2201714. <https://doi.org/10.1002/sml.202201714>.

- [132] Wu D, Tian R, Lin P, Shi ZF, Chen X, Jia MC, Tian YT, Li XJ, Zeng LH, Jie JS. Wafer-scale synthesis of wide bandgap 2D GeSe<sub>2</sub> layers for self-powered ultrasensitive UV photodetection and imaging. *Nano Energy*. 2022;104:107972. <https://doi.org/10.1016/j.nanoen.2022.107972>.
- [133] Ye LY, Zhou SR, Xiong YQ, Tang J, Wang X, Li XD, Pang D, Li HL, Zhang H, Ye LJ, Cui YT, Li WJ. Self-powered Pt/a-Ga<sub>2</sub>O<sub>3</sub>/ITO vertical Schottky junction solar-blind photodetector with excellent detection performance. *Opt Express*. 2023;31(17):28200. <https://doi.org/10.1364/oe.494216>.
- [134] Feng GD, Zhang XX, Tian BB, Duan CA. Retinomorph hardware for in-sensor computing. *InfoMat*. 2023;5(9): e12473. <https://doi.org/10.1002/inf2.12473>.
- [135] Bian HY, Goh YY, Liu YX, Ling HF, Xie LH, Liu XG. Stimuli-responsive memristive materials for artificial synapses and neuromorphic computing. *Adv Mater*. 2021;33(46): 2006469. <https://doi.org/10.1002/adma.202006469>.
- [136] Dutta S, Wilson M. Spatial mapping of distributed sensors biomimicking the human vision system. *Electronics*. 2021; 10(12):1443. <https://doi.org/10.3390/electronics10121443>.
- [137] Chen S, Lou Z, Chen D, Shen GZ. An artificial flexible visual memory system based on an UV-motivated memristor. *Adv Mater*. 2018;30(7):1705400. <https://doi.org/10.1002/adma.201705400>.
- [138] Seo S, Jo SH, Kim S, Shim J, Oh S, Kim JH, Heo K, Choi JW, Choi C, Oh S, Kuzum D, Wong HSP, Park JH. Artificial optic-neural synapse for colored and color-mixed pattern recognition. *Nat Commun*. 2018;9:5106. <https://doi.org/10.1038/s41467-018-07572-5>.
- [139] Kohn A. Visual adaptation: physiology, mechanisms, and functional benefits. *J Neurophysiol*. 2007;97(5):3155. <https://doi.org/10.1152/jn.00086.2007>.
- [140] Kwon SM, Cho SW, Kim M, Heo JS, Kim YH, Park SK. Environment-adaptable artificial visual perception behaviors using a light-adjustable optoelectronic neuromorphic device array. *Adv Mater*. 2019;31(52):1906433. <https://doi.org/10.1002/adma.201906433>.
- [141] Lee TJ, Yun KR, Kim SK, Kim JH, Jin J, Sim KB, Lee DH, Hwang GW, Seong TY. Realization of an artificial visual nervous system using an integrated optoelectronic device array. *Adv Mater*. 2021;33(51):2105485. <https://doi.org/10.1002/adma.202105485>.
- [142] Liao FY, Zhou Z, Kim BJ, Chen JW, Wang JL, Wan TQ, Zhou Y, Hoang AT, Wang C, Kang JF, Ahn JH, Chai Y. Bioinspired in-sensor visual adaptation for accurate perception. *Nat Electron*. 2022;5(2):84. <https://doi.org/10.1038/s41928-022-00713-1>.
- [143] Ho VM, Lee JA, Martin KC. The cell biology of synaptic plasticity. *Science*. 2011;334(6056):623. <https://doi.org/10.1126/science.1209236>.
- [144] Markram H. The blue brain project. *Nat Rev Neurosci*. 2006; 7(2):153. <https://doi.org/10.1038/nrn1848>.
- [145] Shi JL, Jie JS, Deng W, Luo G, Fang XC, Xiao YL, Zhang YJ, Zhang XJ, Zhang XH. A fully solution-printed photosynaptic transistor array with ultralow energy consumption for artificial-vision neural networks. *Adv Mater*. 2022;34(18):2200380. <https://doi.org/10.1002/adma.202200380>.
- [146] Hu YX, Dai MJ, Feng W, Zhang X, Gao F, Zhang SC, Tan BY, Zhang J, Shuai Y, Fu YQ, Hu PA. Ultralow power optical synapses based on MoS<sub>2</sub> layers by indium-induced surface charge doping for biomimetic eyes. *Adv Mater*. 2021;33(52): 2104960. <https://doi.org/10.1002/adma.202104960>.
- [147] Yang XY, Xiong ZY, Chen YJ, Ren Y, Zhou L, Li HL, Zhou Y, Pan F, Han ST. A self-powered artificial retina perception system for image preprocessing based on photovoltaic devices and memristive arrays. *Nano Energy*. 2020;78:105246. <https://doi.org/10.1016/j.nanoen.2020.105246>.

Springer Nature or its licensor (e.g. a society or other partner) holds exclusive rights to this article under a publishing agreement with the author(s) or other rightsholder(s); author self-archiving of the accepted manuscript version of this article is solely governed by the terms of such publishing agreement and applicable law.

